

POLITECNICO DI TORINO

Master of Science in Electronic Engineering

Master Degree Thesis

**Electro-Absorption  
Investigations of Organic  
Photovoltaic Cells and  
Light-Emitting Diodes (OLEDs)**



**Supervisor:**  
prof. Mariagrazia Graziano

**Candidate**  
Marcello D'ASCENZI

**Co-Supervisor:**  
prof. Franco Cacialli

---

ANNO ACCADEMICO 2017 – 2018

# Summary

The work of this thesis was carried out at the London Centre for Nanotechnology, at University College London, during the last six months as a visiting student from Polytechnic University of Turin.

The project consisted in the realisation of a software implementing novel type of measurements related to the electro-absorption spectra of organic semiconductor devices. Since this was my first experience with LabVIEW and with organic semiconductors, the first weeks before starting programming have been spent getting a grasp on this new matters.

After having provided an up and running framework able to characterise these devices, a batch of samples was produced and studied in our laboratories, giving us an idea on the potential of the new program and providing an insight on the analysed materials.

# Acknowledgements

I would like to thank my Professors, Franco Cacialli and Mariagrazia Graziano, for giving me the opportunity to spend six months working in a friendly and experienced group, in a prestigious university, in a lively and outstanding city.

Every person I met in London with no exception helped me surviving my first experience as a European student, especially Ioannis for always being there when an hand was needed.

Rest assured I am not forgetting my Homeland: special thanks go to all my family and friends, being the reasons why in these five years I kept and still keep pushing, even if most of them were distant, it did not feel so.

In particular, two girls did not stop (not even when I did) to have faith in me, my Mother and my Love.

Last, but not least, all my heart goes to my late Grandmother, Grandfather and Father. Even if you did not have the chance to rejoice with me during my experience, I am sure your guidance can still be felt in terms of courage when I think about you.

# Contents

<b>1</b>	<b>Organic Semiconductors Physics Overview</b>	9
1.1	Physics of Conjugated Polymers	9
1.2	Solar Cells	12
1.2.1	Light-Polymer Interactions	12
1.2.2	Bulk Heterojunction Solar Cells Structure	13
1.2.3	Current-Voltage Characteristics of a Solar Cell	15
1.3	Organic Light-Emitting Diodes	16
1.3.1	Working Principles of Light Emission in Organic Devices	17
<b>2</b>	<b>Electro-Absorption System</b>	19
2.1	Electro-Absorption Spectroscopy	19
2.2	Laboratory Set-Up	22
2.2.1	Optical System	23
2.2.2	Measurement Instruments	24
2.3	Example of Electro-Absorption Spectroscopy: Built-In Voltage Determination in Organic Light-Emitting Diodes	25
<b>3</b>	<b>Electro-Absorption Software Development</b>	29
3.1	Main Objectives	29
3.2	LabVIEW Programming	30
3.2.1	Writing the Code	31
3.2.2	Original Laboratory System's Improvements	34
3.3	Main Achievements	36
<b>4</b>	<b>Experiments</b>	39
4.1	Experimental Settings and Studied Devices	39
4.2	Fabrication Techniques	40
4.2.1	Creation of the Layered Structure	40
4.2.2	Solutions' Preparation	42
4.3	Electro-Absorption Characterisation of Bulk Heterojunction Organic Photovoltaics	42
4.3.1	No-PEDOT:PSS Spectra Comparisons	42

4.3.2	PEDOT:PSS Response to Bias . . . . .	43
4.3.3	Frequency Dependence: a Bigger Picture . . . . .	44
4.4	Voltage Dependence . . . . .	46
<b>5</b>	<b>Conclusions</b>	<b>49</b>
5.1	Future work . . . . .	49
<b>A</b>	<b>LabVIEW Electro-Absorption Framework</b>	<b>51</b>
A.1	User Interface . . . . .	51
A.1.1	Main Menus . . . . .	51
A.1.2	Calibration/Alignment Menu . . . . .	52
A.1.3	EAB Spectrum Menu . . . . .	54
A.1.4	Frequency Sweep Menu . . . . .	55
A.1.5	AC Sweep Menu . . . . .	56
A.1.6	DC Sweep Menu . . . . .	57
A.2	LabVIEW Scripts: EAB Measurements . . . . .	57
A.2.1	Front Panel . . . . .	57
A.2.2	Calibration . . . . .	60
A.2.3	EAB Spectrum . . . . .	61
A.2.4	Fq/AC/DC Sweeps . . . . .	62
A.3	LabVIEW Scripts: GPIB Libraries . . . . .	64
A.3.1	Monochromator . . . . .	64
A.3.2	Lock-In . . . . .	65
A.3.3	Multimeter . . . . .	65
A.3.4	Global Variables . . . . .	66
A.4	Post-Processing and Plotting Scripts . . . . .	66
	<b>Bibliography</b>	<b>71</b>



# Introduction

Scientific research in the area of organic semiconductors has spawned many new kinds of devices over the last two decades, and is getting further interest after the promises of these peculiar materials were fulfilled with performing novel technologies and their wide adoption by consumer electronics [1–4].

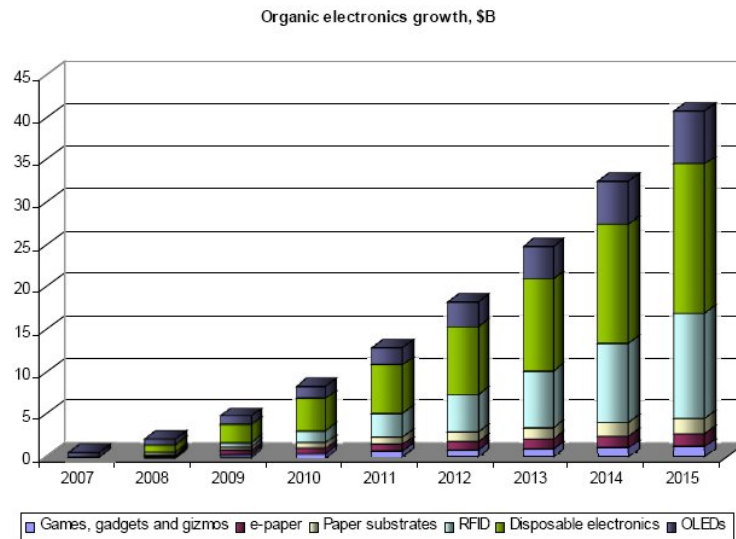


Figure 1: Organic electronics market growth over the years, in billion USD [5].

Organic electronics can be processed in solution, differently from the "classical" photolithographic process. Low manufacturing cost, ease of fabrication and the possibility of building "flexible" devices, together with a relatively good efficiency, are just some of the characteristics derived by this novelty and shared amongst *Organic Light-Emitting Diodes* (OLEDs), *Organic Photovoltaics* (OPV) devices, *Thin Film Transistors* (TFT) and, consequently, *Active Matrix OLED* (AMOLED) displays, and so on. However, the fact that plastic films are not as stable as silicon, which has been extensively studied over more than half a century, is still the main problem with this technology and one of the reasons why the scientific community continues investigating every property that is still hidden by "printable"

---

semiconducting materials; consequently, the research on organic electronics does not only focus on devices' structures and design, but also on aspects of the physical chemistry of the materials.

Within this context, *Electro-Absorption Spectroscopy* (EAB), sometimes known as *Charge Modulated Electro-Absorption Spectroscopy* (CMEAS) or *Stark Spectroscopy*, is a useful tool that can reliably provide, amongst the others, a good estimate of the built-in potential, the excitonic binding energy or the dipole moment and polarisability of excited states in any device made by plastic materials between two electrodes [6–12].

In particular, as explained in this thesis, if we introduce a slight modification on this system making the measurement frequency-dependent, it can also give an insight on the delocalised nature of the so-called charge transfer state in an organic solar cell, a matter that is still under scientific debate [13–15].

This thesis is organised as follows: in [chapter 1](#), a brief overview on the physics of organic semiconductors and devices and their fabrication is given; [chapter 2](#) concerns instead the Electro-Absorption Spectrometer theory and laboratory configuration, while the report on the developed software can be found in [chapter 3](#) (for an in-depth analysis on the program and LabVIEW code, see instead [appendix A](#)). Lastly, [chapter 4](#) shows some experimental results obtained by using the new software functionalities and in [chapter 5](#) a conclusion is presented.

# Chapter 1

# Organic Semiconductors Physics Overview

This chapter begins by briefly defining the properties of organic semiconductors. The characteristics of their energy diagrams and bonding configurations are examined, especially regarding conjugated polymers. In the second section, organic solar cells are considered, thus the interaction between light and polymers is described, and also the conduction of the generated charges in a more complex structure. A brief introduction on organic light-emitting diodes is also proposed at the end of the chapter.

## 1.1 Physics of Conjugated Polymers

Carbon belongs to the IV group of the periodic table of the elements and, is characterised by a ground state electronic configuration of  $1s^2 2s^2 2p^2$ , and is thus tetravalent (which means that the outermost shell only has four electron, and it misses another four electrons to complete the octet). This would, in principle, energetically favour an  $sp^3$  hybridisation of the outer orbitals and the formation of a tetrahedral structure, consisting of four  $\sigma$  bonds with other carbon atoms, likewise other semiconducting materials of the VI group (silicon and germanium).

However, diamond is certainly not the most common allotrope for carbon to be found in nature and, as it will be explained, its electrons' localised nature makes it more like an insulator. Graphite (thus graphene if a single layer is considered) is instead more common and has a different structure, where one of the four valence electrons is instead deployed in a double bond; every carbon atom bonds trigonally with three others and the hybridisation is called  $sp^2$ , the last orbital related to the double bond is instead called  $p_z$  and perpendicular to the plane of the formers. These are labelled as  $\sigma$  and  $\pi$  bonds, the latter being far weaker than the others and more delocalised. Consequently, this kind of structure is more similar to silicon and

germanium, in terms of electron mobility, with respect to the diamond one where all the electrons are almost incapacitated of leaving their strong connection due to single bonds.

It is not without reason that conjugated polymers, characterised by an alternation of single and double bonds between their carbon atoms in a long chain, exhibit strong semiconducting properties deriving from the merging of the delocalised  $\pi$  orbitals into a single manifold.

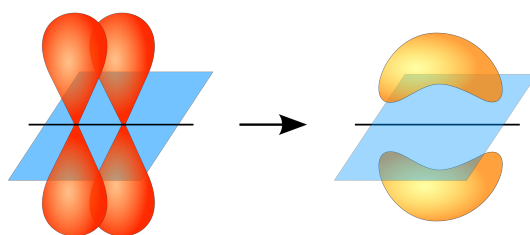


Figure 1.1: Two  $p_{(z)}$  orbitals forming a  $\pi$  bond [16].

By recalling Molecular Orbitals Theory, with the formation of a bond, two states for every bonding electron are created. These are identified as bonding and anti-bonding orbitals ( $\sigma$  and  $\sigma^*$ ,  $\pi$  and  $\pi^*$ ). In silicon and germanium, the formation of the two energy levels for each valence electron and the fact that we have many atoms disposed in an ideally regular lattice give rise to two distinct bands obtained by the superposition of these levels. In the diamond form, the  $\sigma - \sigma^*$  splitting is much bigger than the bands' broadening, making it an insulator. In conjugated polymers, especially for the long-chained ones,  $\pi - \pi^*$  separation can be much shorter and even try approach the "classical" semiconductors' band gap. However, since carbon is in the second period of the table of the elements, its electronegativity is higher than the one of classical semiconductor and its valence electrons are more attracted to the nucleus. The fact that in silicon and in germanium the outer shell is bigger and shielded from the nucleus by many other inner electrons is the main reason why their bandgap is far lower with respect of the one of organic semiconductors, and their conductivity higher.

In general, the energy gap of organic semiconductors is defined as the distance between the Highest Occupied and the Lowest Unoccupied Molecular Orbitals (HOMO and LUMO).

When talking about conductivity in organic materials, care has to be taken. The partial electron delocalisation due to a long conjugation chain does not immediately entail current flow. The different type of lattice, "softer" than a crystal, forces us to a redefinition of the charges, substituted by *polarons*. Polarons are quasiparticles analogous to electrons and holes, with lower mobility and higher effective mass,

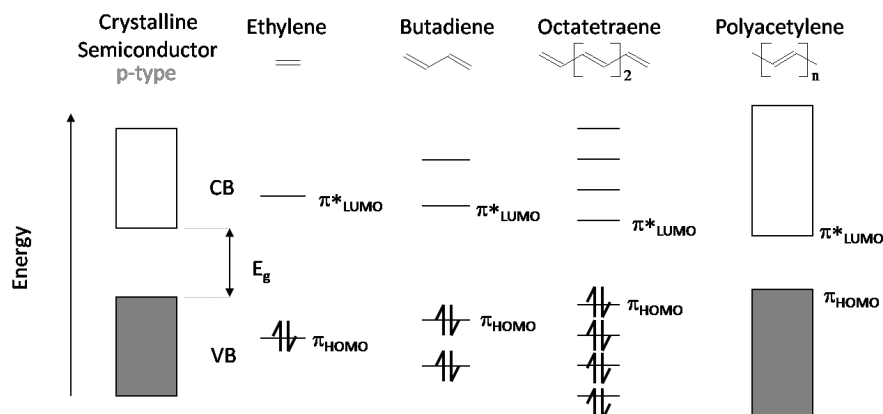


Figure 1.2: Formation of the allowed energies bands in a polyacetylene chain. As we move to the right in the picture, the chain gets longer and the many energy levels introduced start to merge into two bands (adapted from [17]).

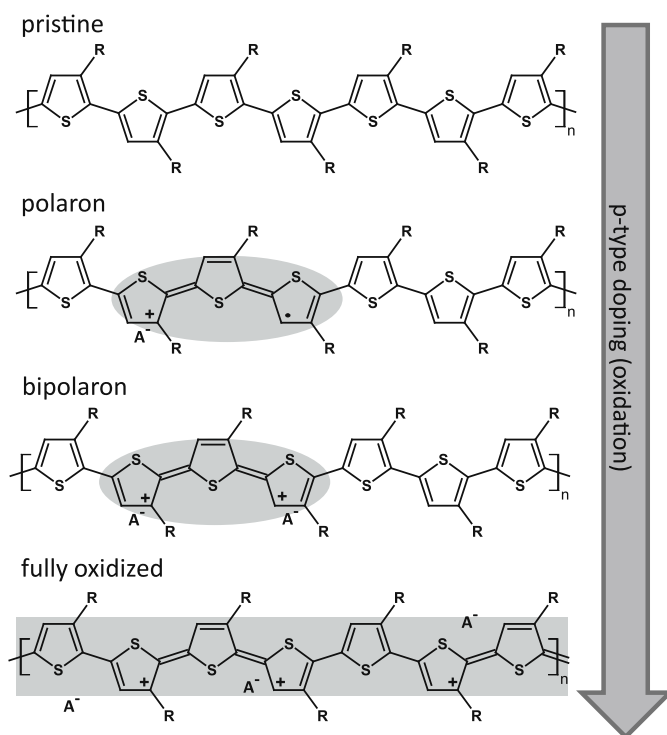


Figure 1.3: Polaron bond configurations in P3HT for different dopings (adapted from [18]).

since they also have to take into account the fact that, for a finite molecule to host a charge, a reshaping is needed. We no longer have fixed atoms that cannot shift from their positions in the lattice, they will have instead to re-adapt to reach a

minimum in energy. In this framework, the polaron moves freely (with its increased effective mass) inside the matrix, that keeps deforming as it passes.

Moreover, these materials' solid state is very different from crystalline semiconductors since the crystal regularity ends with the finite polymer chains of different lengths, and the conduction mechanism is regulated by the *hopping* (a sort of phonon-assisted tunneling) of the polaron from one molecule to another. All in all, the charge transport can be considered dispersive and the mobility is strongly dependent on the electric field ( $\ln\mu \propto \mathcal{E}$ ) [10] and on the available thermal energy.

## 1.2 Solar Cells

### 1.2.1 Light-Polymer Interactions

When an organic molecule interacts with light, it can absorb a photon's energy to give rise to an excited singlet (Fig.1.4). The energy is transferred to one of its electrons that is promoted into an outer energy level, but still maintaining the opposite spin of its paired electron, as in Pauli principle.

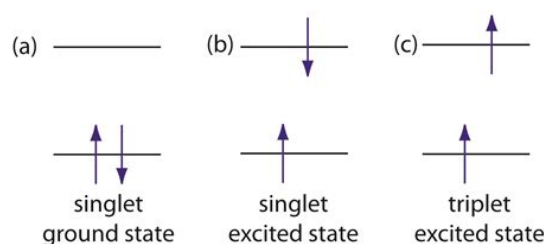


Figure 1.4: Possible electronic states within a molecule. (a): singlet ground state ( $S_0$ ); (b): excited singlet state ( $S_1, S_2, \dots$ ). (c): excited triplet state ( $T_1, T_2, \dots$ ) [19].

The electron-hole couple that is formed in this way is called exciton and, although delocalised, its mobility is relatively low in comparison to its short lifetime, leading to a very small diffusion length. This is also due to the fact that, in conjugated polymers, the dielectric constant is usually low, thus the coulombic interaction is stronger than in inorganic semiconductors.

In Fig.1.5, the Jablonski diagram of organic semiconductors is shown. When an electron is promoted to an higher energy, it almost inevitably becomes an excited singlet. There are many ways in which the excited singlet can decay or mutate (they will be analysed in section 1.3.1), but in solar cells we are interested in collecting the charges at the electrodes that are at the two opposite sides of a structure.

It is important to notice that the incoming light in a polymer can give rise to numerous possible interband transitions, depending on the starting and final energy level (in Fig.1.5 only two absorption lines are depicted, in green straight arrows), so different wavelengths can interact with the molecules.

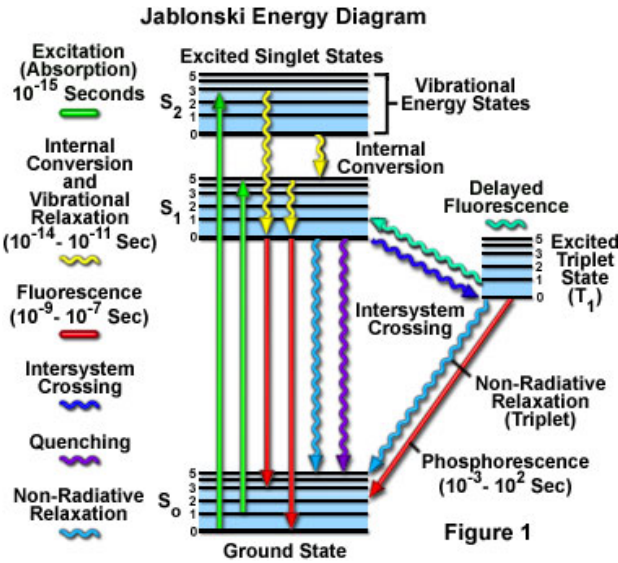


Figure 1.5: An example of Jablonski diagram in organic semiconductors [20].

## 1.2.2 Bulk Heterojunction Solar Cells Structure

In order to improve the charge collection at the electrodes, a straightforward turnaround is employed. Since in normal conditions exciton dissociation would require energies much higher than  $k_B T$  (the thermal energy), the active material is substituted by two different layers with relatively shifted band diagrams (Fig.1.6). If one of the two has a lower LUMO energy level, it will be called electron acceptor. The electron donor is usually instead the material in charge of light absorption. By this particular choice of materials, we facilitate the exciton to dissociate into two opposite charge polarons, breaking the constraining force that was keeping them close, and increasing the mobility of the particles inside the device. Nevertheless, the exciton has to reach the interface to dissociate, so we could still have problems related to diffusion length.

In this way, a good amount of current is extracted from the device under illumination, usually with the aid of an external applied potential, but in principle the band's tilting alone due to the difference in work function of the two electrodes is able to generate a short circuit current. An example of energy levels diagram for this structure is shown in Fig.1.7, where the direction of the two opposite charge flows can also be deduced by the prominent jumps of the energy levels (the ordinate represents the electron potential energy).

The electrodes of the device need to be good conductors and at least one of the two is transparent. The transparent layer is obtained by coating the glass substrate with indium tin oxide (ITO), that can have a  $> 90\%$  transmittance in the visible for a 100 nm deposited layer and resistivity of the order of  $10^{-4} \Omega cm$ . Other transparent conducting oxides (TCOs) can be used, and this terminal is often

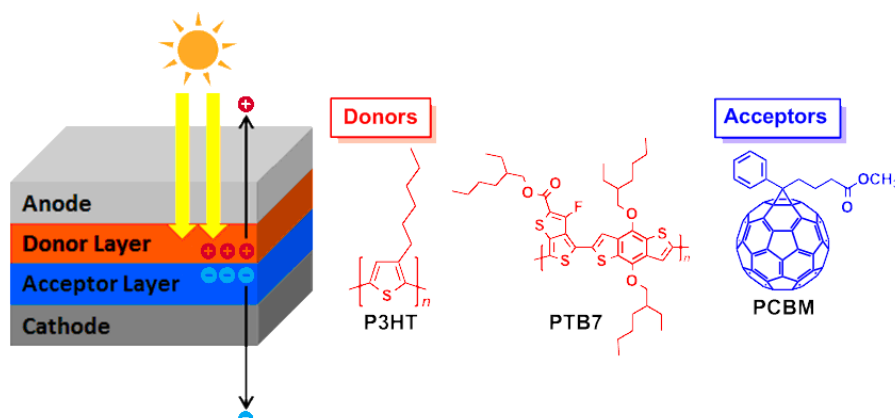


Figure 1.6: An example of an organic solar cell structure and the polymers used for the active layer (adapted from [21]).

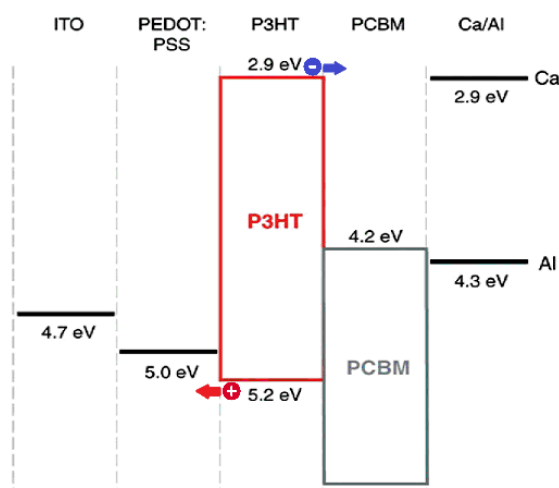


Figure 1.7: Band (energy levels) diagram of an ITO/PEDOT:PSS/P3HT:PCBM/Ca(Al) solar cell (adapted from [22]). The charge flow directions after exciton separation are represented.

considered the anode due to its high work function. However, even if not usual, the *inverted* structure is also possible, where the transparent conductor is used as a cathode and the other dielectric has an even higher work function [23].

In between the anode and the active layer, a hole collecting layer, usually poly(3,4-ethylenedioxythiophene) doped with poly(styrene sulfonate) (PEDOT:PSS), is placed in order to increase the built-in potential of the device and ease the carrier collection at the interface thanks to its excellent hole conductivity and an appropriate HOMO level that can ease the passage of the charges to the electrode [24].

On the opposite side of the active layer, the cathode electrode is present. A

low work function metal is preferred to increase the open circuit voltage of the device and its IV characteristics' filling factor, but this starts to lose meaning if it differs too much from the LUMO value of the acceptor [25]. The choice often falls on aluminium (work function  $\phi \simeq 3.8$  to  $4.1$  eV), calcium ( $\phi \simeq 2.9$  eV) or silver ( $\phi \simeq 4.1$  to  $4.7$  eV). In our case, a thin calcium layer is deposited before a more consistent aluminium one in order to make the energy level transition less steep. When we spread silver paste on the electrodes to generate a connection, the influence on the work function seen by the active layer is negligible due to the thick aluminium layer.

An improvement is possible in this kind of structures if we consider Fig.1.8. We can significantly decrease the mean path that an exciton has to follow before dissociating if we substitute the bi-layer structure with a blend. The entropy of mixing is usually very small for long-chained polymers, and this grants the formation of interpenetrating domains. If the exciton dissociation leaves a polaron free to move inside a domain that is in contact with the right electrode, the charge will be pushed towards that contact, significantly increasing the efficiency of our device.

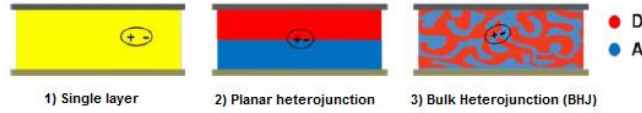


Figure 1.8: Comparison of various active layers [26].

### 1.2.3 Current-Voltage Characteristics of a Solar Cell

From an electric point of view, the current-voltage (I-V or J-V) characteristic of a photovoltaic cell can be modelled using the Shockley equation:

$$J(V) = J_0 \left[ \exp\left(\frac{qV}{k_B T}\right) - 1 \right] - J_{ph}, \quad (1.1)$$

but differently to a diode, the dark current density ( $J_0$ ) is added to  $J_{ph}$ , the photo-generated current density, when the voltage across the device is low. This allows us, for sufficient incoming lights and conversion efficiencies, to venture far into the IV (fourth) quadrant of the current-voltage plane (not the usual I and III quadrants where a diode regularly works) (Fig.1.9).

The fact that the  $I \cdot V$  product yields a negative sign, id est the dissipated Power in the IV quadrant is negative, tells us an electrical energy is being generated (converted from the electromagnetic energy of the incoming light). It easily follows that, the more distant we are from the axes, the more power we will generate.

If we do a good job on the choice of the materials, we can obtain an IV curve that is as nonlinear (and high in current magnitude) as possible on the 4<sup>th</sup> quadrant.

Figure 1.9: Typical J-V curve of a solar cell. Highlighted, the short-circuit current density ( $J_{SC}$ ), the open-circuit voltage ( $V_{OC}$ ), the current and voltage at maximum power ( $J_{MP}$  and  $V_{MP}$  respectively), the maximum power point ( $P_{Max}$ ), and the fill factor ( $FF$ ) [27].

An high absorption photoactive layer can confer bigger short circuit currents for a given light intensity. The electrodes' work functions can firstly determine the open circuit potential, but also the filling factor of the device: a good combination will provide us a current that is very near to  $I_{SC}$  up until a small neighbourhood of  $V_{OC}$  (then, it increases with a steep derivative).

### 1.3 Organic Light-Emitting Diodes

An organic light-emitting diode is a metal/polymer/metal structure able to convert an injected current into emitted light thanks to the radiative decay mechanisms of the polymer. The net efficiencies of this kind of devices can be extremely high compared to production costs, even if some notable limits are still present.

The simplest structure one can think of is the organic diode, in Fig.1.10, where a single polymer is placed in between two electrodes with different work functions. The anode often coincides with the transparent conductor and the cathode's work function is lower by definition (contrary to solar cells). When the three material are put in contact, thermal equilibrium is reached with the flow of electrons from the cathode to the anode. The resulting net charge densities, localised in close proximity to the interfaces, are the cause of the constant band tilting in the inner layer, signifying a built-in electric field is also present throughout the polymer.

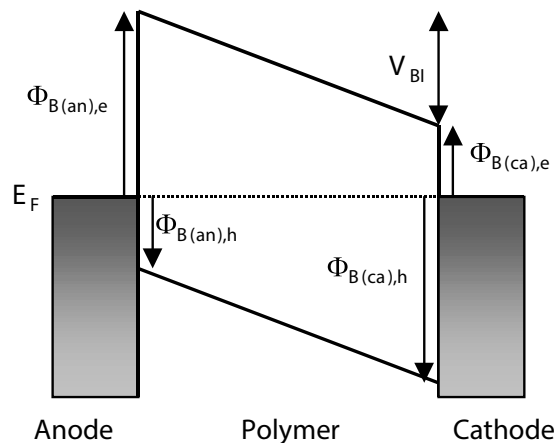


Figure 1.10: Example of organic (light-emitting) diode [10].

### 1.3.1 Working Principles of Light Emission in Organic Devices

When a molecule of the polymer layer is electrically (or optically) pumped into an excited state, we can then incur in different kind of relaxations back into the ground state, and these can be either radiative or non-radiative (Fig.1.5). Differently from decay, apart from rare exceptions, excitation always brings an electron from a HOMO pair (singlet ground state,  $S_0$ ) to form an excited singlet state ( $S_1$ ), that maintains the opposite spin and obeys to Pauli exclusion principle (Fig.1.4 (a) and (b)).

If an excited singlet state directly relaxes into its ground state, this results in a fluorescence emission, having a wavelength that is strictly related to the energy difference of the singlet states ( $E_{ph} \simeq E_{S_1} - E_{S_0}$ ). But if there is a sufficient overlap in vibrational levels, the excited electron can reverse its spin and the state is converted to an excited triplet. This mechanism, called intersystem crossing, is non-radiative and can happen in both directions. The passage from an excited triplet to a singlet ground state can be either radiative or non-radiative. The former is called phosphorescence and usually has a longer time constant and generates photons of longer wavelengths with respect to fluorescence (if we consider the  $S_1$  and  $T_1$  states' decay towards  $S_0$ ). This is also the reason why luminescence in polymers is often represented by two distinct emission spectra (Fig.1.11).

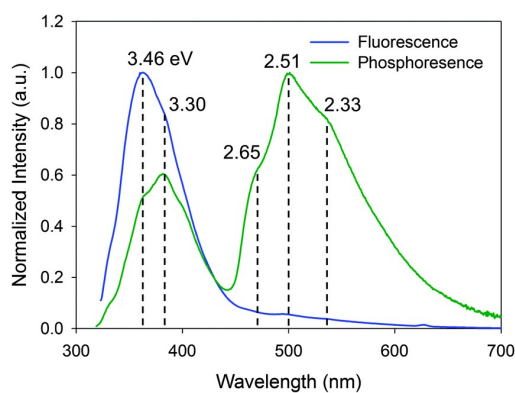


Figure 1.11: Spectra of fluorescence (blue) and phosphorescence (green) in isophthalic acid (IPA) crystals [28].

The ratio between singlet and triplet generation and recombination is actually one of the most limiting factors in OLED efficiency; and is expressed with  $r_{st} < 1$ .

Another efficiency indicator is the *quantum efficiency*  $q < 1$  of a device, representing the probability that the  $S_1 \rightarrow S_0$  exciton relaxation takes place radiatively.

Lastly, we express with  $\gamma < 1$  the ratio between generated excitons and carriers injected in the device. This parameter, called *charge balance*, can be influenced by many factors. Injection barriers, carriers' mobilities and lifetimes all have to be

optimised not to waste the current applied to the device, and this can be obtained with more complex structures (Fig.1.12). In brief, the ample choice that we have in organic polymers (with respect to traditional semiconductors) allows us to create a stratified structure with different properties for every layer. Injecting layers allow us to improve the injection efficiencies, reducing the charge blocking effects of the barriers. Transport layers are characterised by higher mobilities, increasing the diffusion length of the charges. In this way, the exciton formation is more likely to happen in the middle of the device, where we have the emission layer. In some cases, a blocking layer is needed: this can limit current wastes if a charge has a higher mobility with respect to the other (for example, holes reaching cathode terminal) [29].



Figure 1.12: An example of multi-layered OLED structure.

By grouping the aforementioned unidealities, we can obtain the internal quantum efficiency, representing the amount of generated photons inside the device per entering electrons:

$$\eta = \gamma r_{st} q \quad (1.2)$$

## Chapter 2

# Electro-Absorption System

Electro-absorption (EA) spectroscopy is a non-linear optical technique used to reveal physical properties of a layered sample structure through the application of a known applied electric field.

This chapter gives a brief overview of this technique by examining how the materials react to an electric field stimulation first, then it looks at the instruments settings and laboratory procedures. Issues on the system that have been addressed during the writing of this thesis are discussed in later sections.

### 2.1 Electro-Absorption Spectroscopy

EA spectroscopy measures the normalised variation of the transmitted light through a slab under the effect of a periodic electric field [10].

When a light with intensity  $I_i$  is incident on a sample, the transmitted light intensity can be considered (on a first approximation) to be:

$$I_t = I_i(1 - R)^2 e^{-\alpha d}, \quad (2.1)$$

where  $d$  is the distance travelled by the light within the material and  $\alpha$  and  $R$  are the absorption and reflection coefficient. Under the application of an applied electric field  $\mathcal{E}$  to the sample,  $\alpha$  and  $R$  are varied accordingly, leading to:

$$\begin{aligned} \frac{\partial I_t}{\partial \mathcal{E}} &= I_i \left[ -d(1 - R)^2 e^{-\alpha d} \frac{\partial \alpha}{\partial \mathcal{E}} - 2(1 - R) e^{-\alpha d} \frac{\partial R}{\partial \mathcal{E}} \right] = \\ &= -I_i e^{-\alpha d} \left[ d(1 - R)^2 \frac{\partial \alpha}{\partial \mathcal{E}} + 2(1 - R) \frac{\partial R}{\partial \mathcal{E}} \right]. \end{aligned} \quad (2.2)$$

Dividing the field-induced variation by the transmitted (unperturbed) intensity, we obtain:

$$\frac{\Delta T}{T} = \frac{\Delta I_t}{I_t} = -d\Delta\alpha + \frac{2}{1 - R}\Delta R. \quad (2.3)$$

In our case, the second term of 2.3 can be neglected [30], thus the variation of absorption is approximately proportional to the normalised variation in transmitted light:

$$\frac{\Delta T}{T} = -d\Delta\alpha. \quad (2.4)$$

The derivation of the absorption coefficient is not as simple as the previous one.

In the classical electron oscillator model (Lorentz oscillator) the mass of the nucleus is reasonably considered infinite to reduce the system's complexity to a spring-mass problem [31, 32]. Two forces are present in the system of Fig. 2.1 acting on the electron's position  $x(t)$ , a driving force due to the electric field, and the restoring force of the nucleus (behaving as a spring with constant  $k$ ):

$$F_E = -q \cdot \mathcal{E}_x(t), \quad F_k = -k \cdot x(t). \quad (2.5)$$

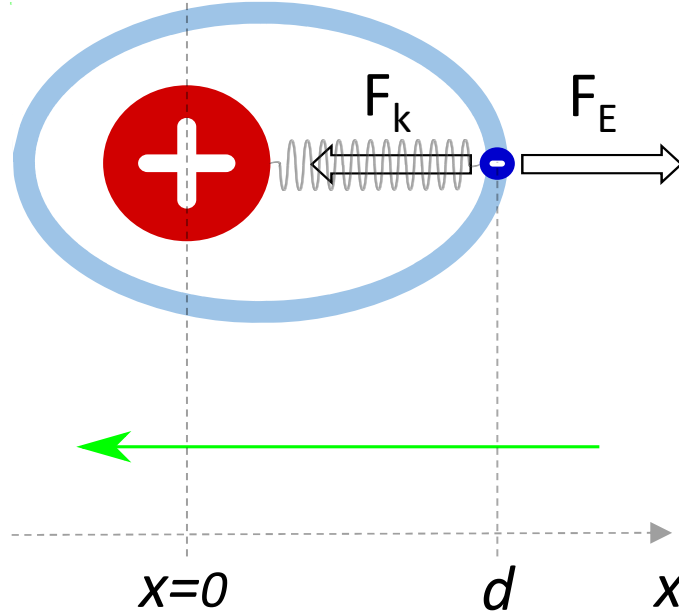


Figure 2.1: Electron oscillator model. The force exerted by the electric field is represented by  $F_E$ , while  $F_k$  is the attractive ( $\simeq$  elastic) force of the nucleus.

The equation of the electron's motion that comes from this free-body diagram,

$$m_e \frac{d^2 x(t)}{dt^2} = -k \cdot x(t) - q \cdot \mathcal{E}_x(t), \quad (2.6)$$

is the one of a classical oscillator with resonance frequency  $w_0^2 = \frac{k}{m_e}$ . The moving of the electron generates a microscopic electric dipole moment  $\mu_x(t) = -qx(t)$ , and we now also know that its response to an external electric field will be the one of an

oscillator. In general, if we consider all the three axes and every atom composing a material, we can define the polarisation vector as the volume density of dipole moments:

$$\vec{P}(t) = V^{-1} \sum_{i=1}^N \vec{\mu}_i(t). \quad (2.7)$$

In general, when a medium is exposed to an electric field, it generates in response of it an electric polarisation that opposes it and is proportional to the  $\chi$  electric susceptibility tensor:

$$\vec{P}(t) = \epsilon_0 \chi \vec{\mathcal{E}}(t). \quad (2.8)$$

The susceptibility is connected in turn to the dielectric displacement  $\vec{D}$  of the media:

$$\vec{D} = \epsilon_0 \epsilon_r \vec{\mathcal{E}} = \epsilon_0 (1 + \chi) \vec{\mathcal{E}} = \epsilon_0 \vec{\mathcal{E}} + \vec{P}, \quad (2.9)$$

and contains the  $n$  refractive index since  $\epsilon_r = n^2 = (n' + in'')^2$ .  $n'$  is the propagation index indicating the phase velocity and  $n''$  is the extinction coefficient, always positive and present if the material has losses (or negative in case of gain). It has to be noted that the  $n''$  sign is only valid for the convention:

$$\vec{\mathcal{E}}(\vec{r}, t) = \mathcal{E}_0 \exp[i\omega (nk_0 \hat{s} \cdot \vec{r} - \omega t)] = \mathcal{E}_0 \exp \left[ i\omega \left( \frac{n' \hat{s} \cdot \vec{r}}{c} - t \right) \right] \exp \left[ \frac{-\omega n'' \hat{s} \cdot \vec{r}}{c} \right], \quad (2.10)$$

otherwise the field would increase as we step away from the source, due to the last exponential ( $\hat{s}$  is the direction of propagation and  $nk_0 \hat{s} = k_x \hat{x} + k_y \hat{y} + k_z \hat{z}$  is the wave vector of the field).

Considering that  $\lambda = 2\pi \frac{c}{\omega}$  and  $I \propto \mathcal{E}^2$ , we can equate the two rightmost exponentials in 2.1 and 2.10, supposing that for the same distance  $l$  we should appreciate the same attenuation, to obtain:

$$\exp[-\alpha l] = \exp \left[ -2 \frac{\omega n'' l}{c} \right] \implies \alpha = \frac{4\pi}{\lambda} n''. \quad (2.11)$$

However, the proportionality between polarisation and electric field (Eq.2.8) cannot be exhaustively described through a linear relationship. For large displacements, the restoring force in the electron oscillator becomes increasingly nonlinear, and this has an impact also on the susceptibility tensor relations. Since we cannot find an exact solution for our system, the best way to analyse it is by expanding the susceptibility or, better, the polarisation as a Taylor series in  $\mathcal{E}$  [33]:

$$P = \epsilon_0 \left( \chi^{(1)} \mathcal{E} + \chi^{(2)} \mathcal{E}^2 + \chi^{(3)} \mathcal{E}^3 + \dots \right), \quad (2.12)$$

where the tensor form has not been used for notational reasons and  $\chi^{(n)}$  is the  $n^{\text{th}}$  order susceptibility tensor.

The second order term  $\chi^{(2)}$  vanishes in centrosymmetric materials (such as many conjugated polymers' backbones) since we expect the polarisation to change sign when the field is reversed. Moreover, it is very difficult to observe responses of order higher than the third [34]. Therefore, we can rewrite Eq.2.12 as:

$$P = \epsilon_0 \chi \mathcal{E} = \epsilon_0 \left( \chi^{(1)} + \chi^{(3)} \mathcal{E}^2 \right) \mathcal{E}, \quad (2.13)$$

We can express the variation of susceptibility due to a change in electric field as:

$$\Delta \chi = \chi - \chi_0 = \left( \chi^{(1)} + \chi^{(3)} \mathcal{E}^2 \right) - \chi^{(1)} = \chi^{(3)} \mathcal{E}^2, \quad (2.14)$$

and from 2.9 we also notice that  $\Delta \chi = \Delta \epsilon_r$ . Since also  $\epsilon_r = n^2$ , considering Eq.2.14, we have:

$$\Delta \chi = 2n \Delta n \implies \chi^{(3)} = \frac{2n \Delta n}{\mathcal{E}^2}. \quad (2.15)$$

Now, we know from 2.4 how to evaluate the absorption coefficient  $\alpha$  from the normalised variation of transmitted light  $\frac{\Delta I_t}{I_t}$  and from 2.11 how to connect it to the extinction coefficient  $n''$ . If we use it together with the Kramers-Kronig relations we obtain:

$$\Delta n'(\omega) = \frac{2}{\pi} \int_0^\infty \frac{\omega' \Delta n''(\omega')}{\omega'^2 - \omega^2} d\omega' = \frac{c}{\pi} \int_0^\infty \frac{\omega' \Delta \alpha(\omega')}{\omega'^2 - \omega^2} d\omega'. \quad (2.16)$$

We can use the relation in Eq.2.16 to find also  $n', n''(\alpha)$ , i.e. a relation between the absolute refractive index and absorption coefficient.

Thus, the third order non-linear susceptibility  $\chi^{(3)}$  can be evaluated from a Kramers-Kronig analysis of the electro-absorption and absorption spectra of the device. Materials with a large third order susceptibility component have many applications in the field of nonlinear optics [34], and conjugated polymers usually exhibit an high  $\chi^{(3)}$  as a result of their "elongated"  $\pi$  bonds.

## 2.2 Laboratory Set-Up

One of the most common way to apply a test field to a polymer, as done in this thesis, is to employ a layered "vertical" structure, similar to the one in section 1.2.2, where the two electrodes enclose the polymer layer. We can apply an arbitrary voltage (alternate and continuous components) to the electrodes to generate an electric field inside the material while illuminating it with a focused light beam (of constant intensity) through the transparent conductor. The light will then be reflected by the second electrode, that can be considered as a perfect mirror for our range of frequencies, and will leave the device with a modulated intensity. If the beam is focused towards the device with a  $45^\circ$  angle, as shown in figure 2.2, we can easily direct the output into a photodiode for measurements.

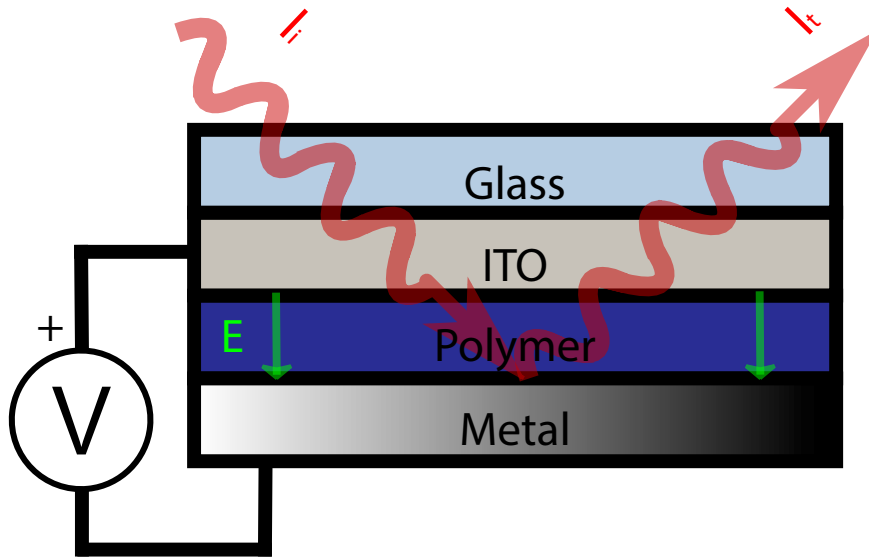


Figure 2.2: Schematic of the device under test. In red, the incoming and outgoing light. In green, the electric field generated by an external voltage source.

### 2.2.1 Optical System

A simple schematic of the set-up, showing also the light's path, is shown in Fig.2.3.

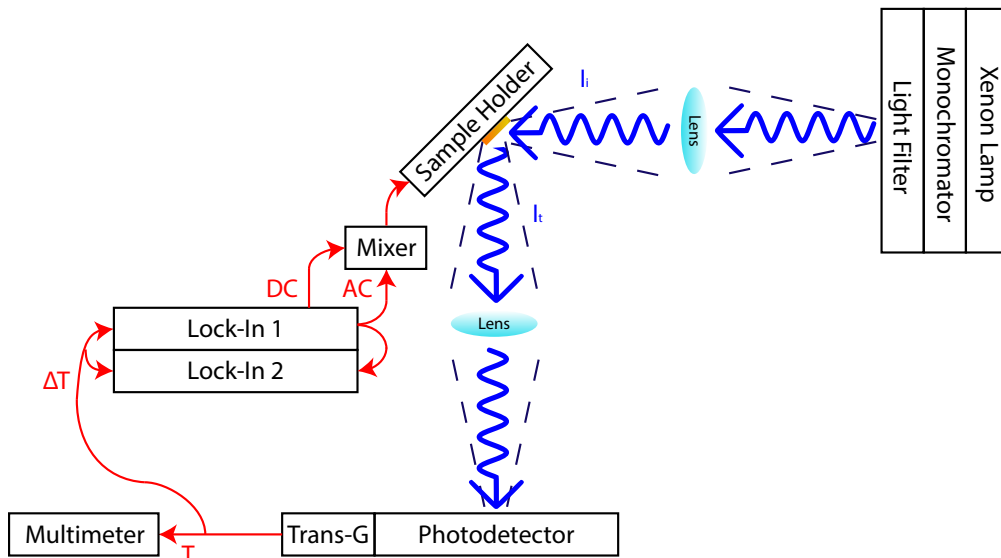


Figure 2.3: Electro-absorption laboratory Set-Up.

The light is generated by an SL-03730 300W short arc xenon lamp, providing a polychromatic illumination (as shown in Fig.2.4). In order to make it suitable

for our experiment, it has to be guided into and processed by a Bentham TMc300 monochromator, that will isolate a narrow band of the spectrum around a selected wavelength. The tested instrument was reasonably accurate around the range 200 – 900  $nm$ . The device employs mechanically adjustable diffraction gratings to make only a small interval of wavelengths resonate within its structure, acting as a very selective anti-reflective coating. Before exiting its output slit, if needed, an additional long-pass optical filter can be used to attenuate higher orders of diffraction ( $\lambda_2 = \lambda_F/2$ , where  $\lambda_F$  is the filtered wavelength, could also be transmitted, even if with a low attenuation).

Along the path that goes from the output slit to the sample holder, the spot size of the beam will keep increasing unless we place a converging lens between the two. If the reflecting contact of the sample is near enough to the focal point of the system, we can limit the losses in resolution due to diffraction. The same has to be done for the reflected light going into the photodetector.

The detector, a Hamamatsu Photonics S1406 photodiode, has an operating wavelength range going from 190  $nm$  to 1  $\mu m$ . A transconductance amplifier is included in the package, in order to keep the feedback resistor as close as possible to the sensor because of the importance that noise level has in the measurement. The signal is then sent to the lock-ins and the multimeter via a shielded coaxial cable.

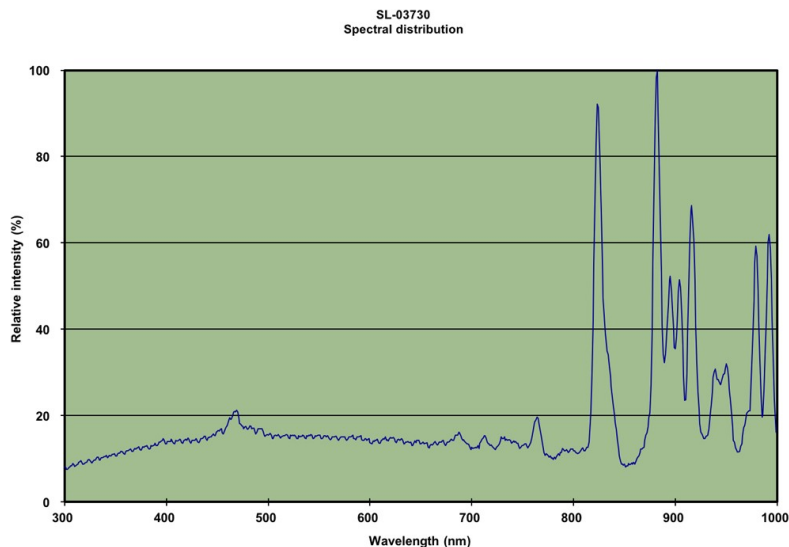


Figure 2.4: SL-03730 xenon lamp spectrum [35].

## 2.2.2 Measurement Instruments

The Keithley Model 199 multimeter is in charge of measuring the direct component of the light beam. Its input reading is set to voltage because of the photodetector's

transconductance amplifier. Although the signal has an AC component, its magnitude is so small (compared to the average intensity of the incoming light) that is already filtered out as a noise by the multimeter.

That is the reason why Stanford Research Systems SR830 lock-in amplifiers have been chosen. Knowing the carrier of a signal, they can isolate and measure it even if well below the noise wall, as in this case. The reference signal is generated by one of the lock-ins, and is used both to modulate the electric field inside the sample and as an internal reference. The second lock-in uses it to generate its second harmonic and use that as an external reference. The first auxiliary output port of the first lock-in is also used to provide a constant voltage. The latter, and the AC signal are sent to an additive mixer.

The mixer sums up the AC and DC components coming from the first lock-in and sends the resulting system to the sample electrodes. As explained in section 3.2.2, software corrections have been carried out to the reference phases to correct the fact that the mixer inverts the incoming signals while summing them.

## 2.3 Example of Electro-Absorption Spectroscopy: Built-In Voltage Determination in Organic Light-Emitting Diodes

Using a semiclassical approach, the electro-absorption problem can be studied through Stark effect to characterise the dependence of  $\alpha$  on the applied electric field. In general, the electro-absorption proportionality coefficients can be modelled as a linear combination of the absorption and its first and second derivatives with respect to the incident photons' energy:

$$\frac{\Delta T}{T} \propto \left[ a\alpha + b\frac{d\alpha}{dE_{ph}} + c\frac{d^2\alpha}{dE_{ph}^2} \right] \mathcal{E}^2. \quad (2.17)$$

Especially in conjugated polymers the weight of the second derivative is related to the degree of disorder in the film and higher order derivatives are usually not considered [6]. This quadratic dependence on the field is crucial when trying to determine the built-in voltage of a device.

When we apply a sinusoidal voltage plus an offset to an electrode/polymer/electrode device, we obtain:

$$V = V_{DC} + V_{AC}\cos(\omega t) \implies \mathcal{E} = \mathcal{E}_0 + \mathcal{E}_{AC}\cos(\omega t), \quad (2.18)$$

noticing also that the constant component of the electric field inside the inner layer does not only depend on the DC bias, instead:

$$\mathcal{E}_0 = \mathcal{E}_{DC} - \mathcal{E}_{BI}, \quad (2.19)$$

the constant component feels the influence of the built-in field  $\mathcal{E}_{BI}$  (or the equivalent voltage  $V_{BI}$ ), that is present in the device at thermal equilibrium. This happens because the two electrodes' work functions are different, and it takes a charge exchange between them to balance the Fermi energies and reach thermal equilibrium at the moment when the heterojunctions are created. The charge that is stored at the interfaces generates this internal field.

However if we consider the proportionality of the spectrum on the field inside the device (Eq.2.17), the relation is not linear:

$$\frac{\Delta T}{T} = \chi(E_{ph})\mathcal{E}^2 \propto V^2, \quad (2.20)$$

where  $\chi(E_{ph})$  is the spectral dependency.

If we substitute the field in Eq.2.20 with Eq.2.18, we can notice that this non-linearity generates second harmonic content:

$$\begin{aligned} \frac{\Delta T}{T} &= \chi(E_{ph}) \left[ \mathcal{E}_{AC}^2 \cos^2(\omega t) + 2\mathcal{E}_{AC}\mathcal{E}_0 \cos(\omega t) + \mathcal{E}_0^2 \right] = \\ &= \chi(E_{ph}) \left[ \mathcal{E}_{AC}^2 \frac{1 + \cos(2\omega t)}{2} + 2\mathcal{E}_{AC}\mathcal{E}_0 \cos(\omega t) + \mathcal{E}_0^2 \right] \end{aligned} \quad (2.21)$$

With our laboratory settings, we are easily able to measure the two harmonic components of the electro-absorption:

$$\left. \frac{\Delta T}{T} \right|_{\omega} = 2\chi(E_{ph})\mathcal{E}_{AC}\mathcal{E}_{DC}\cos(\omega t), \quad (2.22)$$

$$\left. \frac{\Delta T}{T} \right|_{2\omega} = \chi(E_{ph})\mathcal{E}_{AC}^2 \frac{\cos(2\omega t)}{2}. \quad (2.23)$$

Independently (on a first approximation) on  $\chi(E_{ph})$ , we can use the relation in Eq.2.22 to find the bias voltage that sets the electro-absorption signal (and consequently  $\mathcal{E}_0$ ) to zero. This is possible, from Eq.2.19, if the generated DC field evens out with the built in field ( $\mathcal{E}_{DC} = \mathcal{E}_{BI}$ ) or in other terms, we are applying a voltage that is equal to  $V_{BI}$ .

In reality, even the lock-in resolution loses its virtue when approaching the zero of the EA signal. Furthermore, strong charge injections can occur at positive bias voltages, interfering with the uniformity of the electric field inside the polymer, or we could even have electroluminescence phenomena [7]. This results in an highly nonlinear and unreliable  $\frac{\Delta T}{T}$  signal for positive biases, therefore a linear fitting of the values in the reverse bias region is preferred to approximate the zero crossing point (Fig.2.5).

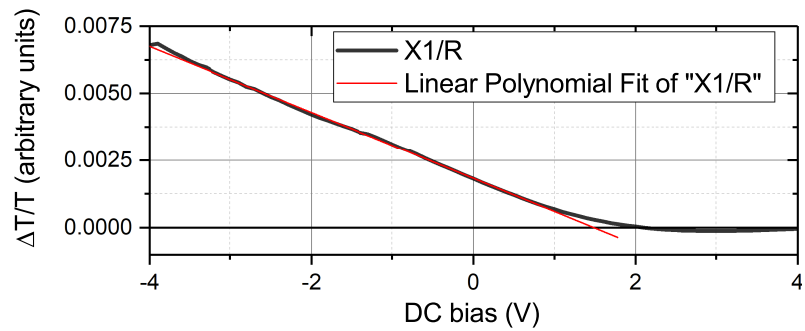


Figure 2.5:  $V_{BI}$  analysis of an  $ITO/PEDOT : PSS/P3HT : PC_{60}BM/ Ca/Al$  device. The built-in voltage is approximated to 1.478 V after a linear fitting of the bias voltage values between  $-3$  V and 0.5 V.



## Chapter 3

# Electro-Absorption Software Development

This chapter will contemplate the software section of the thesis, that is the creation of a LabVIEW library able to handle the electro-absorption system and implement different kind of measurements, from the simple spectrum to 3D (two variables) plots. The program had to rely on low level IEEE488 commands sent through a GPIB to the measurement instruments, and to provide a user-friendly front panel. Most of the graphs were instead produced using MATLAB, OriginPro and Python.

The choice of *G* as a programming language (id est LabVIEW "Graphical" language) was not only dictated by its capability to manage the interface bus, or motivated by the previous members of the research group. The LabVIEW platform was chosen in order to make it easier to understand and modify for the next users to come. Even if its graphical nature makes the code easily readable, an in depth user manual has been attached to the thesis in [appendix A](#), that can also serve as a guide, if the program ever needs improvements or plug-ins, while this chapter will focus on the project requests and the methodologies of development.

### 3.1 Main Objectives

The tasks I had been assigned, regarded the creation of some complex measurement routine, taking the first cues from some basic GPIB instrument drivers that were already present. The "precursor" of the program was a simpler electro-absorption script where, after fixing the operating parameters, the monochromator would sweep through various filtered wavelengths while a lock-in and the multimeter were in charge of taking measurements at every step, producing a spectrum. Another routine was present, in a different library, that could measure the EA signal for different applied voltage bias, and use them to estimate the built-in voltage, as in section [2.3](#).

Unfortunately, at the time the code was written, the developer did not consider code reuse as one of the main intents, so the LabVIEW virtual-instruments (VIs) were not particularly structured, albeit doing their job.

One of the main assignments' purpose was to rewrite the spectrum routine in order to make it easier to be read and modified. As explained in subsection 3.2.1, most of the work consisted in reordering the main functions in a hierarchical structure, being careful to keep the sub-VI as general as possible, as they could make a good frame also for other measurements. Some important adjustments had to be made to the software, detailed then in the subsection 3.2.2, that was not robust enough. In fact, some of these lapses could result in measurement errors that would not account to an "inexpert" user. Some noteworthy improvements at this stage, were the correction of the phase shift errors due to the signal mixer and of the second harmonic measurement, since the instruments were not properly configured to correctly behave under varied working conditions.

After having figured out how the whole system worked (and fixed most of the issues) a "calibration" toolbox was requested, able to perform an instruments inspection while aligning the light beam and the devices, in order to quickly estimate if the signal to noise ratio was sufficient for our experiments and if, by any means, if increasing it was still possible by prudent manoeuvres. Even if an articulate version of this VI was developed, we decided to put in the final program only an abridged one, able to send handy commands and return convenient readings from the instruments at the beginning of the experiments.

Following this, I was requested to create a new VI able to measure, for some fixed wavelengths, the frequency, oscillator AC voltage and DC bias voltage *sweeps*. After some developments, this became the *3D sweep* that is described in the appendix, and is now the main feature of the new program. The reason for this was to have means for investigating in depth the changes happening along the whole spectrum for some parameter's variations.

Lastly, having all the programs ready, I had to design a user-friendly interface that could also be developer-friendly in case integration with other VIs was needed. The front panel had to give access both to the instruments' readings and a menu for choosing the desired measurement and its control variables.

As a side-project, I also developed some more comprehensive VIs tailored to execute all the measurements that I needed in series, and I added an e-mail notification option in order to shorten the time-consuming process in the laboratory.

## 3.2 LabVIEW Programming

Since the available time to produce a functioning software was not insufficient, but still limiting, a software development methodology had to be chosen to optimise the schedule.

The used approach was inspired by the *Manifesto for Agile Software Development* [36], one of the most popular standards in the programming industry. The way of proceeding was really similar. We started with a clear idea in mind, that was to lay a solid basis for the framework by organising all the programs in a hierarchical fashion and by initially creating all the basic sub-blocks. We continued by writing the first complete VI, namely the *EA spectrum*, but then we decided to slow down and to pair my programming sessions to frequent brainstorming, resulting into systematic new ideas and weekly deadlines.

Every step of the process can be seen as a running train: while its wheels keep spinning around their axis indefinitely, the train is indeed going forward. In the same way, each programming cycle consists of starting from a new idea, implementing it from the already produced software and, lastly, thinking about further modifications while testing the new version (Fig.3.1). Consequently, the program is functioning at every step and can be used to take measurements; these measurements will help us isolate possible bugs or inaccuracies, or they will inspire new functionalities or improvements.



Figure 3.1: The agile software development methodology. After the initial project, the plan gets modified from time to time [37].

### 3.2.1 Writing the Code

#### GPIB Library

In the first step of the process, a collection of all the instrument drivers was needed by the program, organised in a clear way and, possibly, optimised in terms of generality and time performance (see for reference section A.3 of the appendix). Focusing on these aspects allows these subVIs to be inherited by higher classes in the hierarchy, or mixed together to form an articulate interface command. An example is shown in Fig.3.8: when possible, the basic instructions are shared between multiple VIs, in this case the *frequency sweep* and the final program. They were separated depending on the specific instrument and, while the K199 multimeters were already available, most of the others had to be built. Then, when needed,

they were collected into bigger blocks, as the more complex ones for instruments' initialisation (Fig.3.2) or range calibration. Ultimately, they were all stored into a *.llb* file, organised in folders.

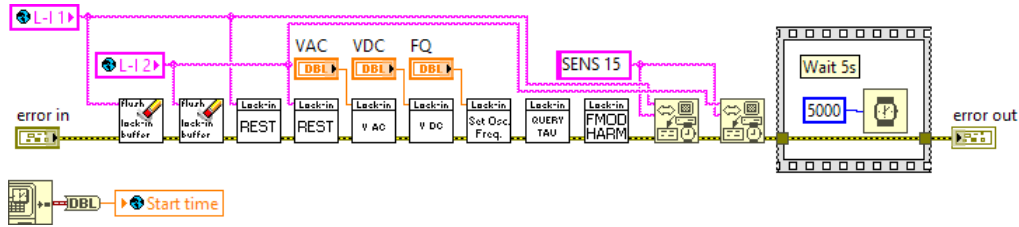


Figure 3.2: Lock-ins' initialisation sequence, as in *Lock-In\_initialize.vi*.

Since some of the instruments had no GPIB read options, or sometimes in order to avoid constantly asking for the same parameters, global variables had to be used (section A.3.4) so that we could store, for example, the monochromator's state or the lock-ins' time constant in a memory element to be shared between different VIs. Another example is the one in Fig.3.3, where all the GPIB addresses are stored altogether in the same global VI, so that every GPIB call makes reference to the same variable, and if we change the address settings of some instruments the program is up to date with the change of a number. It has to be noted that the introduction of global variables can lead to an increase in complexity during code maintenance, so it has been used sparingly but, especially when merging more than one measurement routine inside the same VI, they can relieve the code of bulky constructs.



Figure 3.3: In *Global\_Addresses.vi*, all the GPIB addresses are stored into global variables.

## EAB spectrum

The *EAB spectrum* routine, as shown in A.2.3, was then programmed by taking advantage of the laid foundations. While for the data dump and plotting some efforts have been made, the measurement section can be summed up in a single loop if we employ inherited subVIs (Fig.A.21).

All the *.txt* files are in TSV (tab-separated values), which is a well-recognised format for both OriginPro and MATLAB *datastore*, where every post-processing step is handled. The file names, as well as the headers, are automatically generated

starting from the measurement parameters and at every step the monochromator's wavelength, photodetector's reading from the multimeter and first and second normalised harmonic signals from the lock-ins are stored into a new line.

### Calibration

At the start of an experiment, one has to carry out an alignment step, during which the instrument readings are monitored. The program that assists the user during this process is detailed in section A.2.2 and makes again use of the same GPIB calls as the others.

Originally, some dialogue windows guided the user through a step-by-step configuration and a buzzer could be configured to signal if a certain threshold was reached. The final version of the program, anyway, only contains the essential indicators.

### Two-Parameters Sweeps

A more complex version of the spectrum routine was then requested. The reason was that we wanted to investigate the frequency dependence of the excitonic peak of a material and compare it to the one of the charge transfer state. This could give an idea on the delocalised nature of a certain state rather than another (see section 4.3). So, in principle, the program had to take a frequency sweep at two chosen wavelengths and compare them. However, we found it interesting that also for other wavelengths a sometimes different frequency dependence could be noticed, so we decided to add some degrees of freedom to the measurement parameters. The array containing the two wavelengths became an equispaced generated vector and, all in all, we were measuring the frequency dependence of the whole EAB spectrum. As an example, in Fig.3.4 and Fig.3.5 we can see the frequency analysis of a device having *P3HT : PC<sub>60</sub>BM* as polymer layer. Both the *X* and *Y* signals of the first harmonic are plotted and their behaviour is quite different: as the frequency increases, the in phase component oscillates near to a point while the quadrature component reverses its sign, resulting in an almost constant magnitude (even if slightly decreasing) and a change of phase in the signal.

Other two versions of the *3D sweep* are also present now, where the frequency has been substituted with the DC bias voltage and the oscillator AC voltage. These could in principle allow to find interesting deviations from the predicted dependences of the EA signal to the fields applied to a device.

### User Interface

After all the VIs were ready, a repository was needed, and we decided to keep using LabVIEW to merge everything into a single program. All the previously existing scripts became libraries supporting the main one.

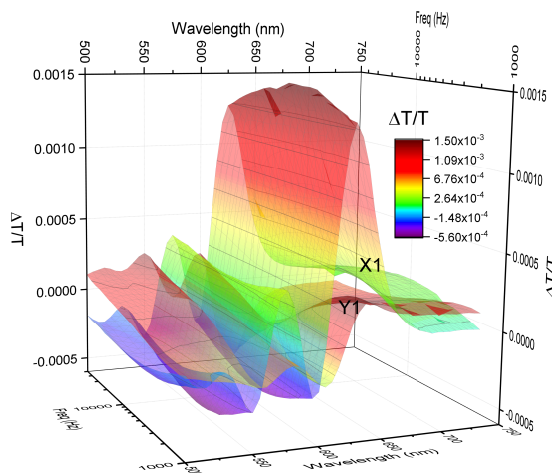


Figure 3.4: 1<sup>st</sup> harmonic X and Y 3D plot of a P3HT:PC<sub>60</sub>BM sample’s frequency sweep.

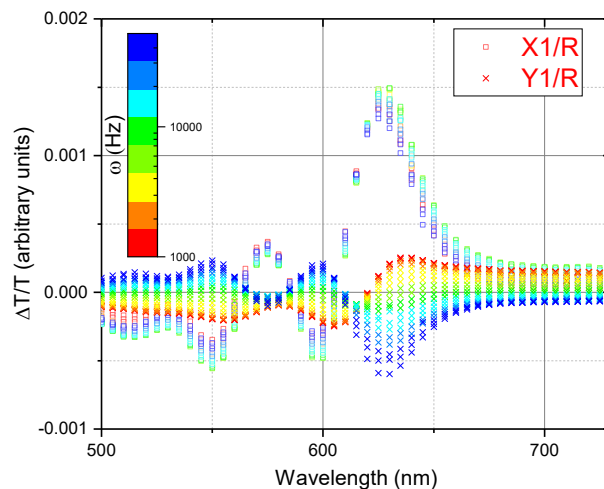


Figure 3.5: 1<sup>st</sup> harmonic X and Y colour plot of a P3HT:PC<sub>60</sub>BM sample’s frequency sweep.

The user interface is organised in directories leading to the desired measurements (section A.1). This will allow any future add-on to be easily inserted in the structure. Care has been taken while adding utilities to the front panel, such as the e-mail notifications and the completion percentage indicator, in order to help the user optimise his time while taking measurements.

### 3.2.2 Original Laboratory System’s Improvements

The system and the laboratory set-up had to be optimised for the new measurements at the beginning, and some of the issues still were not addressed for the already available software.

#### Monochromator Interface

One of the main flaws of the system previously designed was the monochromator’s management. The actual wavelength had to be written into a text file before starting the program and, if the execution was interrupted before completion, the file had to be manually updated with the reached point (the same was valid for the filter position). This inconvenient feature was obviating the fact that there is no way to read from the monochromator.

This has been improved using global variables and user prompts (Fig.A.1 and Fig.A.2) so that, after asking for the parameters once, their values are stored for as long as LabVIEW is running.

### Phase Inconsistencies

The lack of a proper initialisation in the code was the source of a hidden measurement error on the phase of the readings; put together with the fact that the signal mixer, while adding DC and AC components together, was also inverting created then some confusion on the phase settings of the lock-in, that have never been fixed. The DC voltage was inverted before being sent to the mixer, but no care had been taken of the AC signal (Fig.3.6).

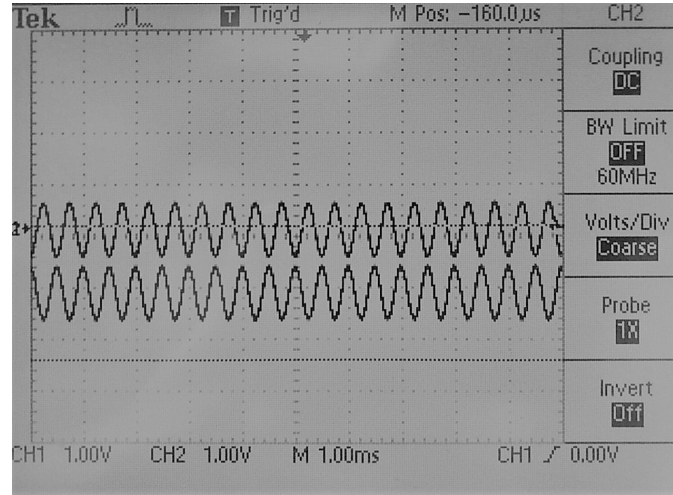


Figure 3.6: The signal before (at 0  $V_{DC}$ ) and after (at -1  $V_{DC}$ , opposite in phase) the mixing.

To understand the problem, let us consider how the two lock-ins work. The one that is generating the first harmonic, compares the photodetector signal to its oscillator to read, ideally, an in phase and a quadrature components, that could be seen in phasor form as an amplification (or attenuation) and a phase shift components:

$$R_{L-I}/\phi_{L-I} = \frac{v_{PD}}{v_{osc}} = \frac{A \cdot V_{osc}/\phi_{osc} + \Delta\phi - 180^\circ}{V_{osc}/\phi_{osc}}, \quad (3.1)$$

where  $A$  and  $\Delta\phi$  are the amplification and phase shift changes introduced by the device and the  $-180^\circ$  shift is due to the mixer. Since we would like to read  $R_{L-I}/\phi_{L-I} = A/\Delta\phi$  we can add to the oscillator, during the input demodulation, an analogous  $-180^\circ$  phase shift that will cancel out the previous inversion, so that we have the correct reading.

The same procedure has not to be taken with the second lock-in since, as we can see from Eq.2.23, the second harmonic is proportional to the square of the applied field, thus it is insensitive to the AC signal inversion. In this case, a  $-180^\circ$  phase shift in the reference would introduce a sign error. *Lock-in\_Phase\_Initialise.vi* fixes this issue at runtime by forcing the reference phases to  $-180^\circ$  and to  $0^\circ$  respectively for the first and second lock-ins.

### Lock-In Autorange

Lock-in amplifiers are precision instruments, thus require to work under ideal conditions to give the best results. One of the conditions has to do with the full-scale range ( $FSR$ ). If the input signal of an instrument is as close as possible to the  $FSR$  (and vice-versa), we can reduce the error of a measurement. For this reason, efforts have been made so to choose the right  $FSR$  while keeping the time wastes contained (Fig.3.7).

Since the lock-in library does not contemplate a suitable autorange function, a simple iterative one has been designed, where each time the input intensity (modulus  $R$ ) is compared to the  $FSR$ , and a sensitivity adjustment is performed if out of a certain interval. Otherwise, an *hit counter* is increased and we leave the function after a certain number of *consecutive hits*. The loop also ends after a certain *max iterations* number, so that we are sure not to end up stuck in a time consuming process due low signal to noise ratios.

## 3.3 Main Achievements

The electro-absorption laboratory framework was tuned-up and enlarged with new functionalities during my experience. Some of them added original features to the programs, now able to take different kind of measurements, some others helped the overall performance by reducing execution times and robustness of the routines.

One of the main accomplishment resides in the fact that the system is now much easier to use. Furthermore, its speed has been significantly increased while maintaining the same accuracy: now it is possible to study (both EA and 3D analysis of) two different devices during the same workday while it was almost impossible beforehand. One of the most time-consuming process, anyway, remains the placing of the sample inside the sample-holder in the glovebox and its alignment in the EA laboratory.

As we will see, the 3D plots of the devices' response give us a broader view on the electro-absorption properties of the materials and help us detect subtle deviances from the expected behaviour if present. This ability is of the utmost importance when studying novel materials we still do not know much about.

The code is now structured in a way that can help the next users better understand how the measurements work, and the graphical interface pleasantly collects all the work done in a single, convenient, front panel.

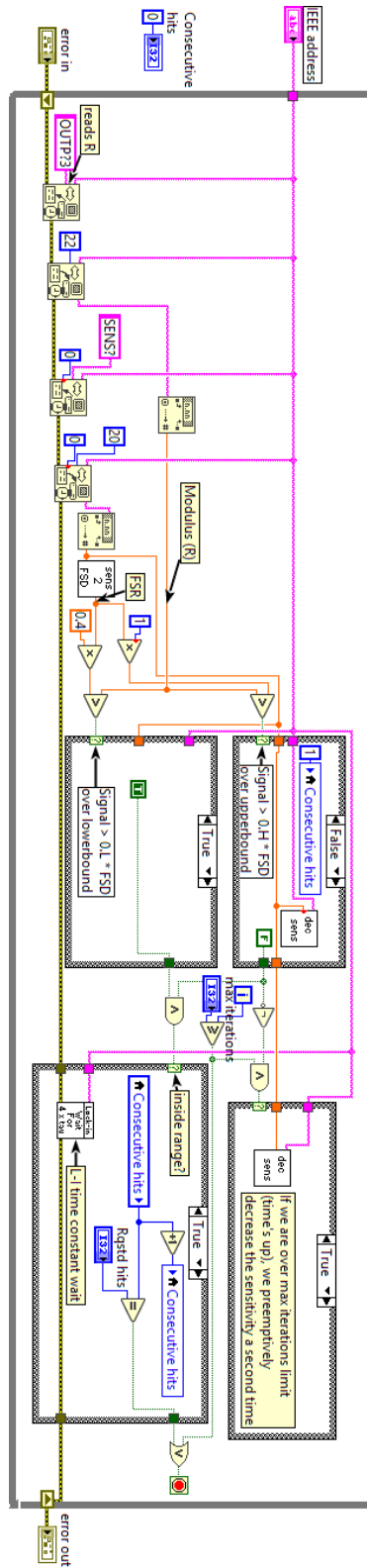
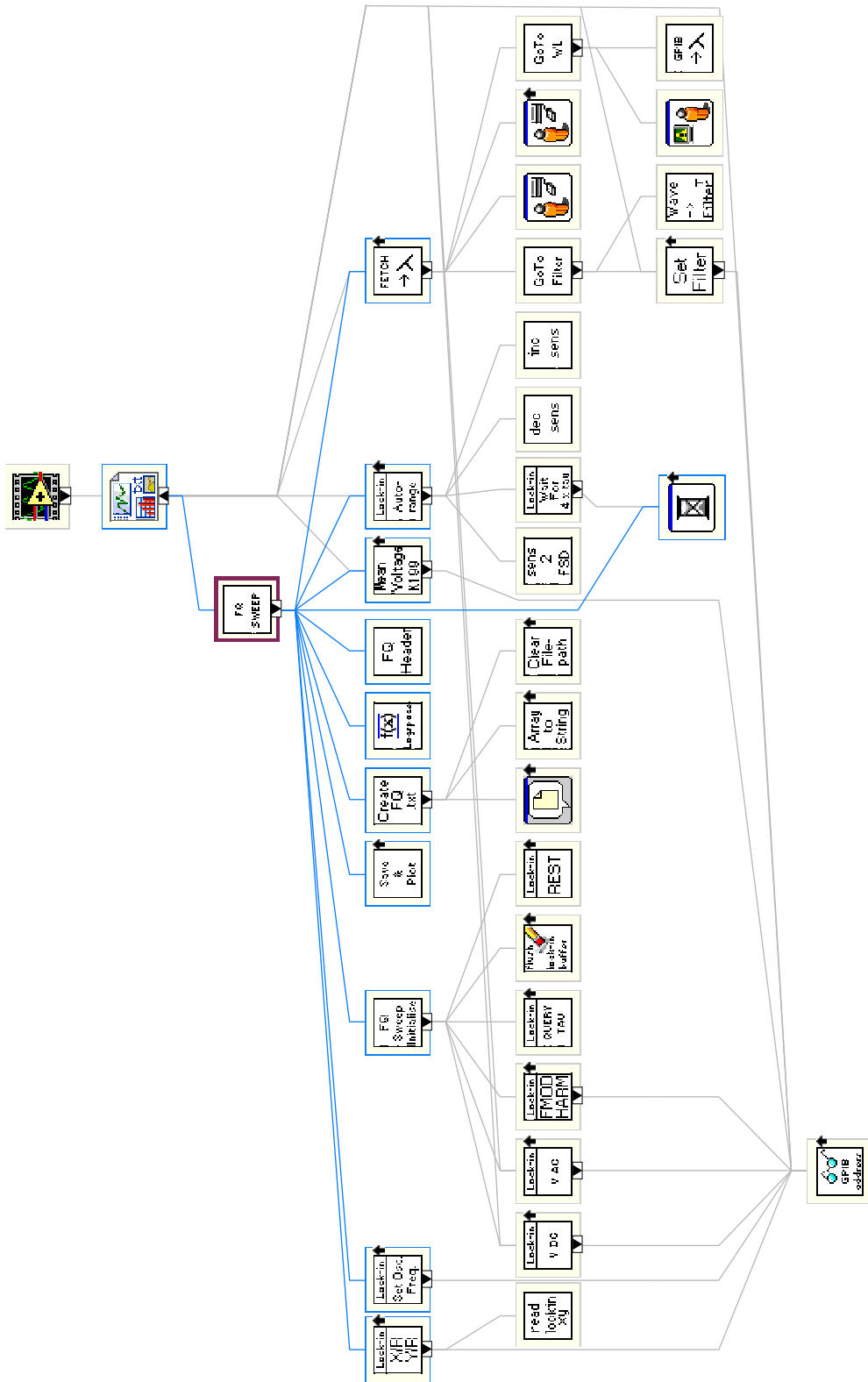


Figure 3.7: *Lock-In\_Autorange.vi*.



# Chapter 4

## Experiments

After the description of the electro-absorption system, in chapter [chapter 2](#), and of the program, in chapter [chapter 3](#) and [appendix A](#), the next crucial point, treated in this chapter, will be its testing and validation during the study of organic semi-conductors.

We will start by describing the aim of the experiment, the studied devices and their fabrication. Then, the data will be analysed and compared to recent literature to check if the results are reliable.

### 4.1 Experimental Settings and Studied Devices

We decided to explore the new functionalities of the program by fabricating and testing a batch of organic solar cells with ITO as cathode and calcium and aluminium (deposited one after the other) as anode. Every device of the batch had differences in fabrication steps or inner layers' materials with respect to the others.

In particular, we wanted to study the effects of the introduction of poly(3,4-ethylenedioxythiophene):polystyrene sulfonate (PEDOT:PSS) in organic solar cells with different active layers. PEDOT:PSS is often used as a protection layer to prevent diffusion of anode molecules into the active layer, causing device degradation due to the formation of charge trap centres. It also acts as an electron-blocking layer, giving a huge boost in efficiency in bulk heterojunction devices, where electrons can be generated by exciton dissociation even if we are near to the anode [11].

The batch of samples was divided in three groups of five:

- **Active layer:** the simplest samples, to act as a reference, had only a polymer (or blend) between the two electrodes.
- **PEDOT:PSS + active layer:** devices with a PEDOT:PSS layer amidst cathode and active layer, as already discussed.

- **Annealed PEDOT:PSS + active layer:** before the active layer was deposited, a thermal annealing step has been performed in these devices.

Thermal annealing of PEDOT:PSS has been reported to slightly increase  $J_{SC}$  (while also slightly decreasing the filling factor), probably thanks to the decrease in surface roughness of the material, enabling the creation of a smoother contact [38].

For the active layers, three different polymers have been used, two electron donors and one acceptor. The donors were Poly(3-hexylthiophene) (*P3HT*) and Poly[[4,8-bis[(2-ethylhexyl)oxy]benzo[1,2-b:4,5-b']dithiophene-2,6-diyl][3-fluoro-2-[(2-ethylhexyl)carbonyl]thieno[3,4-b]thiophenediyl]] (*PTB7*). The acceptor was [6,6]-phenyl-C-61-butyric acid methyl ester (*PC<sub>60</sub>BM*). Along with them, we also studied their donor-acceptor blends (*P3HT:PC<sub>60</sub>BM*, *PTB7:PC<sub>60</sub>BM*). In total, 15 devices were produced.

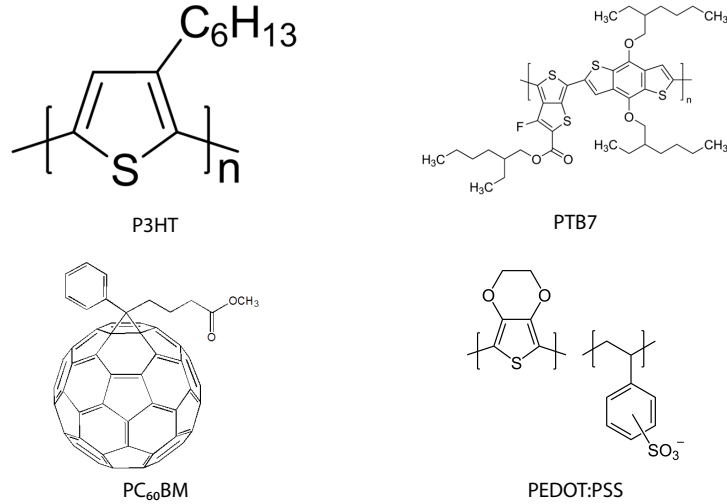


Figure 4.1: A list of all the structural units of the polymers employed in the devices. It has to be noted that PC<sub>60</sub>BM, differently from the others, is not a polymer and is not characterised by a repetition unit.

## 4.2 Fabrication Techniques

### 4.2.1 Creation of the Layered Structure

In solution processed deposition, the polymer is dissolved into a solution and is deposited on top of the previous film through spin coating, drop casting or even ink-jet printing. In our experiments, after preparing the solutions, we used spin coating to deposit the films. In this technique, the substrate of the device is vacuum sealed to a base that starts rotating after we deposit the solution. The solvent

will start to evaporate while also being flung off the sides, until we reach a final thickness that will mostly depend, apart from solution properties, on the angular velocity of spinning. The layers formed with this technique can be as thin as tens of nanometres [39]. The characteristics and concentrations of the prepared solutions are discussed later in section 4.2.2.

We started from ITO coated glass substrates that went through a 15 minutes washing (water, acetone, IPA) and a 20 minutes oxygen plasma cleaning step. We proceeded by depositing 200  $\mu\text{l}$  of PEDOT:PSS (if the device contemplates it) and spin coating it for 300 seconds at 6000 *rpm*. The solution was formerly filtered with a 0.45  $\mu\text{m}$  PVDF membrane filter. Some of devices were then left inside the glovebox (in nitrogen atmosphere) to anneal for 150°C for 45 minutes. After allowing it to rest, the other polymers were spin coated on top of the devices, this time by depositing 80  $\mu\text{l}$ , then leaving them to spin at 1000 *rpm* for 2 minutes. These solutions were filtered with a 0.45  $\mu\text{m}$  PTFE membrane filter instead.

After that, the devices were moved to the evaporator to deposit, in sequence, 20 *nm* of calcium and 100 *nm* of aluminium. The mask used for the sputtering were tailored to create three long and thin cathode contacts on top of the device and leave an empty space on a side of it. The empty space was there to allow for an incision on the polymers, so that we have a trench to reach the ITO with a contact. We then used a silver paste to connect the electrodes to the probes of the sample holder via an ohmic contact.

The final schematic of a fabricated bulk heterojunction solar cell is shown in Fig. 4.2. The vertical dimension is emphasised.

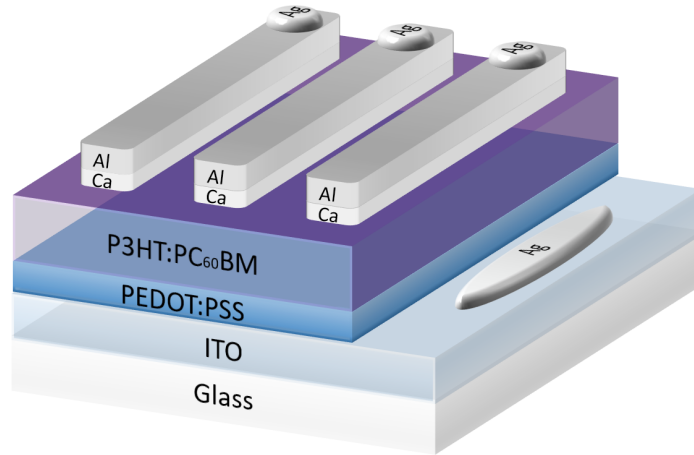


Figure 4.2: Studied sample configuration for an ITO/PEDOT:PSS/P3HT:PCBM/Ca/Al solar cell. The silver paste contacts are spread manually after having scratched a side of the active layer.

## 4.2.2 Solutions' Preparation

As already discussed, spin coating requires the polymers to be in solution. The used solvent was 1,2-Dichlorobenzene (DCB). We prepared 0.5 ml for every solution, with a concentration of approximately  $25 \frac{mg}{ml}$ , sufficient for the creation of 15 samples.

For the pristine devices, 12 mg P3HT, PTB7 and PC<sub>60</sub>BM were added in vials, each containing 0.5 ml of solvent.

PTB7:PC<sub>60</sub>BM simply needs a 1:1 ratio of its components for making the blend, thus 6 mg each were added in 0.5 ml of solvent. P3HT:PC<sub>60</sub>BM needs instead an higher concentration by weight with respect to PC<sub>60</sub>BM, of 1:7, so we used 7.68 mg of P3HT and 5.378 mg of PC<sub>60</sub>BM.

The solution were left to stir overnight before employing them for the fabrication of the devices.

## 4.3 Electro-Absorption Characterisation of Bulk Heterojunction Organic Photovoltaics

### 4.3.1 No-PEDOT:PSS Spectra Comparisons

We started testing the program and the new devices by comparing the electro-absorption spectra of the no-PEDOT:PSS samples batch.

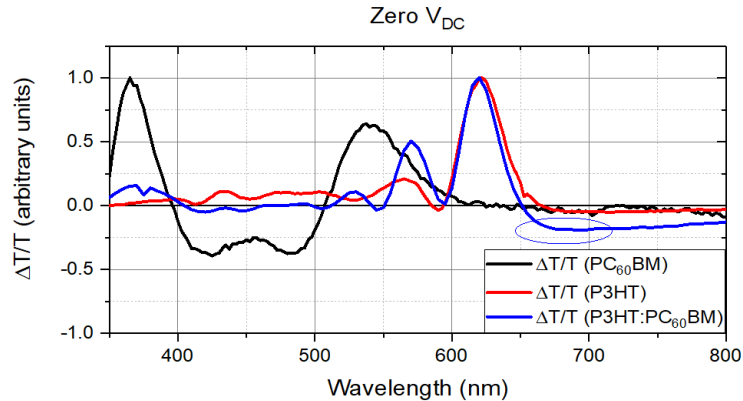


Figure 4.3: Comparison between no-PEDOT:PSS devices normalised EA spectra. Pristine P3HT and PC<sub>60</sub>BM samples are shown, along with their blend with its sub-bandgap feature emphasised.  $V_{DC} = 0 V$ ,  $V_{AC} = 1 V$ ,  $f = 2 kHz$ .

The pristine materials spectra follow the expected behaviour, in particular the P3HT one has its more prominent peak around the wavelength of 620 nm, where its excitonic contribution is expected to be. If we do a comparison between P3HT, PC<sub>60</sub>BM and P3HT:PC<sub>60</sub>BM samples, as in Fig.4.3, we can notice that the blend

device’s spectrum seems to follow the peaks of both the pristine ones (the influence of P3HT being predominant), with one exception: for wavelengths that are longer than 620 nm (*i.e.* lower photon energies), it exhibits a feature that is not present on any of them. This sub-bandgap interaction is thought to be an effect of the charge transfer (CT) state, formed when we separate an exciton at the interface between donor and acceptor materials. The energy that separates the pair is now lower, since it corresponds to the interaction between an hole in the HOMO of P3HT and an electron in the LUMO of PC<sub>60</sub>BM.

The same happens in no-PEDOT PTB7 and its blend with PC<sub>60</sub>BM, with the only difference being the fact that its energy gap and CT state are located at lower energies (Fig.4.4).

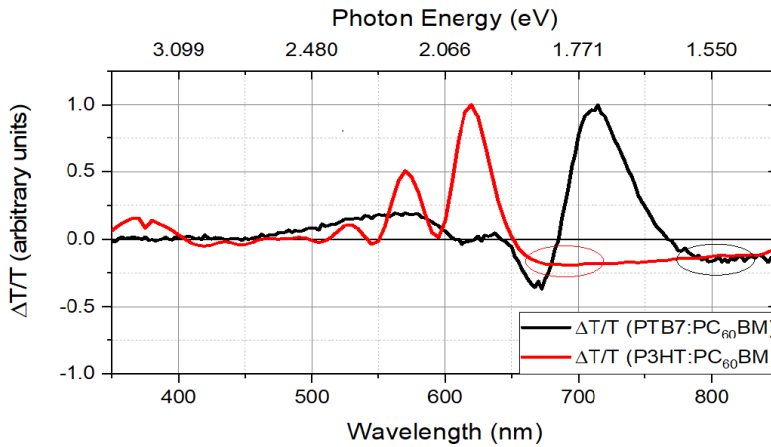


Figure 4.4: Comparison between no-PEDOT:PSS devices normalised EA spectra. PC<sub>60</sub>BM blends all exhibit peculiar sub-bandgap features, as emphasised.  $V_{DC} = 0 V$ ,  $V_{AC} = 1 V$ ,  $f = 2 kHz$ .

### 4.3.2 PEDOT:PSS Response to Bias

By comparing different devices with a P3HT:PC<sub>60</sub>BM active layer, we could see the difference in behaviour, in particular of CT state, that is obtained when adding PEDOT:PSS to our layered structure (Fig.4.5, Fig.4.6).

With no applied bias the excitonic and CT states do not show evident differences when a PEDOT:PSS layer is added to the device (Fig.4.5). If we apply a  $-2V$  negative bias (Fig.4.6), the whole spectrum undergoes a change of shape and the excitonic peaks experience a red shift. The surprising fact, anyway, is the complete disappearing of the CT state with the negative bias, that only happens when the protection layer is present. It is still unclear how PEDOT:PSS interacts with the rest of the device, but this effect could be due to a state introduced by it, cancelling out with with CT state in an interference only present at negative biases.

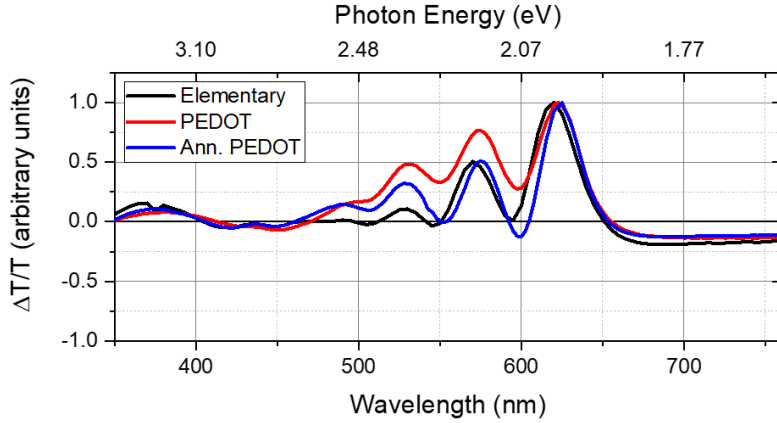


Figure 4.5: Comparison between P3HT:PC<sub>60</sub>BM blends normalised EA spectra. The CT states show no significant variations with zero applied bias.  $V_{DC} = 0 V$ ,  $V_{AC} = 1 V$ ,  $f = 2 kHz$ .

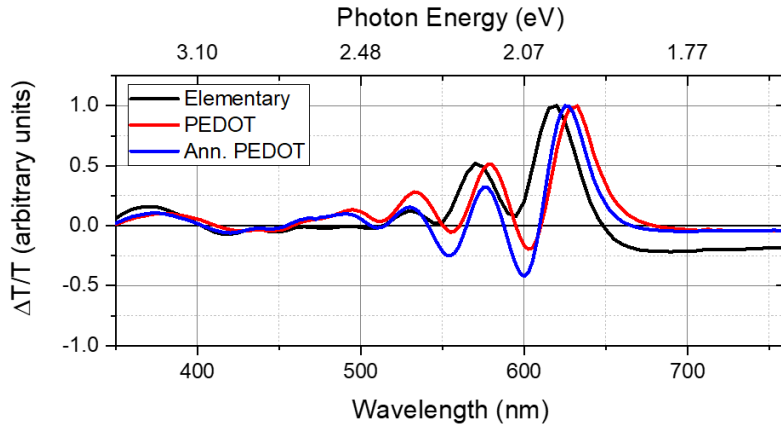


Figure 4.6: Comparison between P3HT:PC<sub>60</sub>BM blends normalised EA spectra. We can notice a suppression of CT state with negative applied bias when PEDOT:PSS is present.  $V_{DC} = -2 V$ ,  $V_{AC} = 1 V$ ,  $f = 2 kHz$ .

### 4.3.3 Frequency Dependence: a Bigger Picture

By exploiting the potentialities of the new tools, we can have an interesting and more general overlook on the response of the fabricated devices with respect to frequency. If we take a frequency sweep of the whole spectrum, the differences in behaviour between charge transfer and excitonic states become more evident.

As we can see in Fig.4.7, when PEDOT:PSS is not present in P3HT:PC<sub>60</sub>BM devices, the EA response oscillates around the same values and is characterised by a small resonance peak for frequencies that are slightly lower than  $10 kHz$ .

If PEDOT:PSS is added to the structure, anyway, an evident change in behaviour

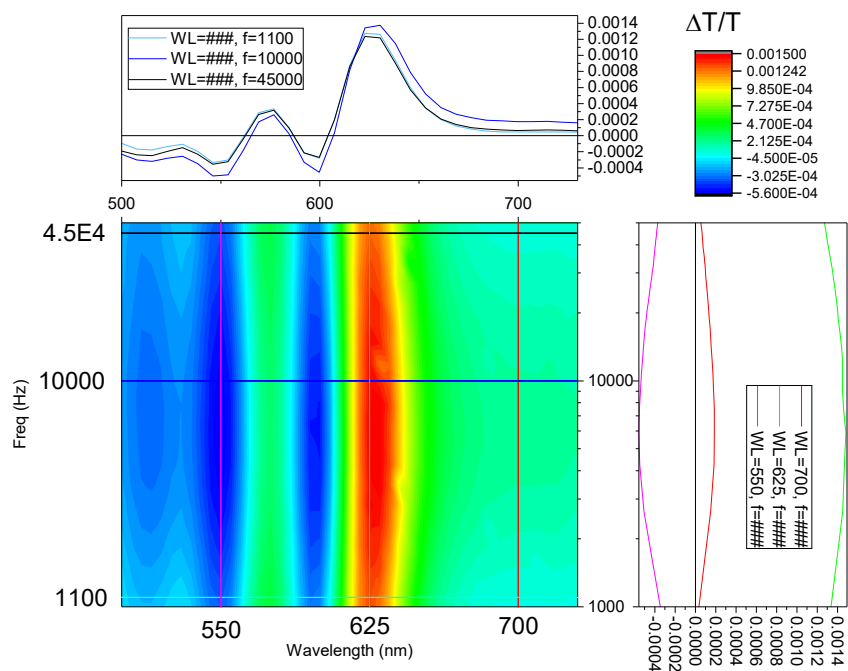


Figure 4.7: P3HT:PC<sub>60</sub>BM, contour plot of the 3D frequency sweep.

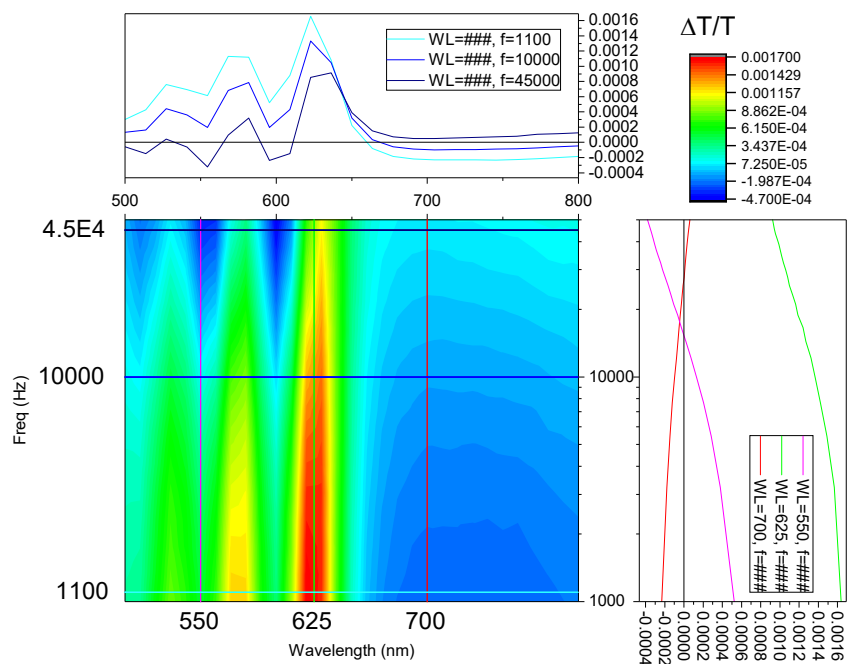


Figure 4.8: PEDOT:PSS/P3HT:PC<sub>60</sub>BM, contour plot of the 3D frequency sweep.

is present. The trend of the frequency dependence becomes monotone for any fixed frequency and, sometimes, even a change in sign is present. All in all, the results seem to converge to the previous sample when the frequency exceeds 10  $kHz$ . This could mean that PEDOT:PSS is responsive up to a limited frequency, and only after its cutoff we start to see the CT state alone. As suggested by Guan *et al.* [13], the PEDOT:PSS could introduce in the device an interfacial polaron state that, contrary to the CT state, is strongly localised and unresponsive to high modulation frequencies. This could clearly explain also the fact that for an high frequency the spectrum resembles the one when no PEDOT:PSS is present.

Furthermore, this behaviour is also present for PTB7:PC<sub>60</sub>BM devices, even if to a lesser extent, as it is shown in Fig.4.9.

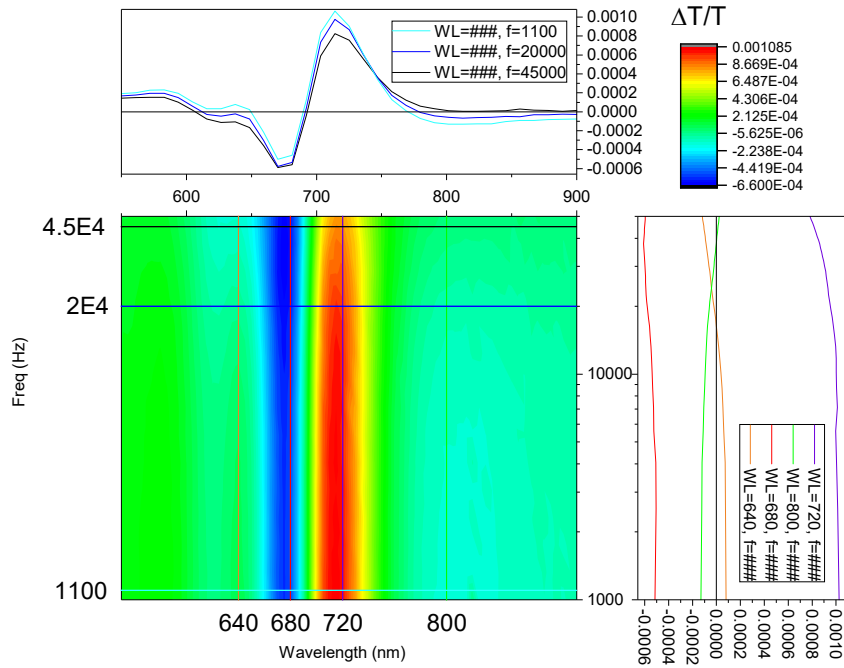


Figure 4.9: PEDOT:PSS/PTB7:PC<sub>60</sub>BM, contour plot of the 3D frequency sweep.

## 4.4 Voltage Dependence

As already discussed, the bias dependence can be influenced by the presence of PEDOT:PSS. In Fig.4.10, both the excitonic and the CT states of P3HT:PC<sub>60</sub>BM devices have been studied while changing the structure. When PEDOT:PSS is added to the device layers, no significant changes are present for the response of the excitonic state: the trend stays monotonically decreasing while passing from reverse to forward bias, with just a little less attenuation when the additive layer is present.

The CT state instead, is noticeably different. If for a reverse bias the simpler devices has a stable negative voltage, for the PEDOT:PSS one the signal approaches the zero as we increase the negative voltage. If we instead invert the direction of the bias, the result is the exact opposite: the PEDOT:PSS device shows an increase of EA signal, while the other one goes to zero.

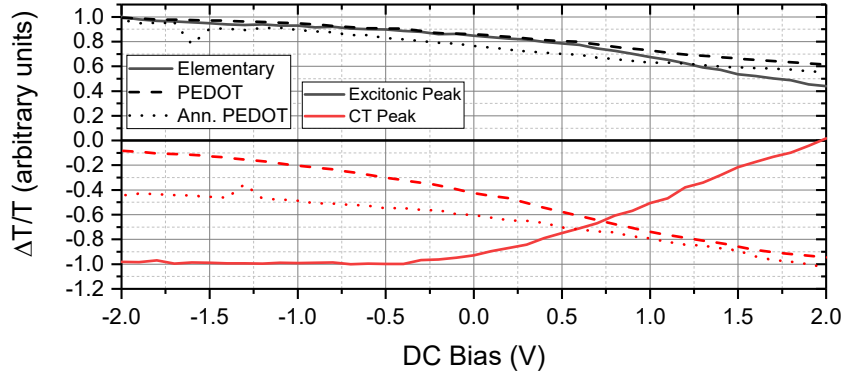


Figure 4.10: DC Sweep comparison in different P3HT:PC<sub>60</sub>BM devices.  $V_{AC} = 1 V$ ,  $f = 2 kHz$ .

The AC sweep comparison does not appear to show remarkable differences in the trends (Fig.4.11). Anyway, when PEDOT:PSS is present, the response seems to follow a straighter line. This means that it follows in a clearer way the expected behaviour from Eq.2.22.

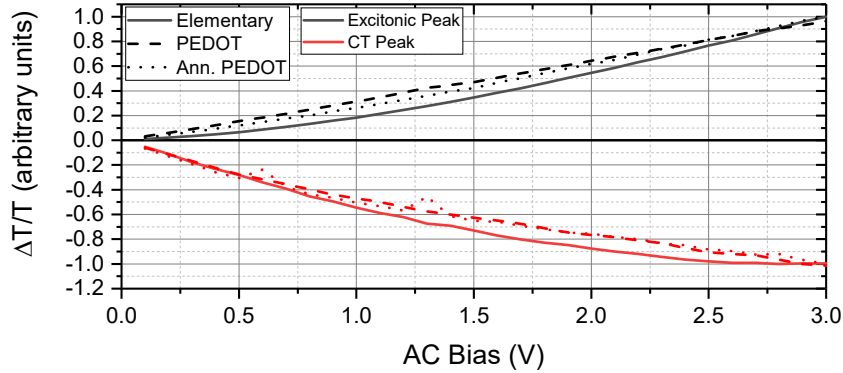


Figure 4.11: AC Sweep comparison in different P3HT:PC<sub>60</sub>BM devices.  $V_{DC} = 0 V$ ,  $f = 2 kHz$ .



# Chapter 5

## Conclusions

During this thesis, a performing LabVIEW electro-absorption framework was developed. The main design constraints and specifications were met, providing a user-friendly software able to make new kinds of measurements.

The laboratory times were substantially improved by making the GPIB commands simpler and by adding new features, such as a calibration and alignment tools and e-mail notifications.

The new measurement routines helped us identifying hidden deviations from the theory in the responses of the materials. In particular, we were able to discriminate between the polaronic state (introduced by PEDOT:PSS) and the charge transfer state responses to a varying modulation frequency, and to ascertain the delocalised nature of the latter.

### 5.1 Future work

Unfortunately, the fact that we managed to study only a batch of 15 devices did not suffice for rigorously probing new materials' properties. Some more samples are needed also to check if the results were not only anecdotal, and we hope that future test will confirm our findings.

However, on account of the fact that this was only a preliminary attempt to test the program, it is hardly surprising that we are still waiting to inspect different samples before confirming our theories or formulating novel ones. The dependence of PEDOT:PSS devices response on voltage bias still has to be investigated in depth to be understood, and it can only be done by testing different kind of structures.

Moreover, we are confident that the program will help us study new materials. Perovskite and magnesium oxide layers will be studied in solar cells and this could lead to the writing of new papers.



# Appendix A

## LabVIEW Electro-Absorption Framework

The aim of this *User Guide* is not only to show how to set and use this program, but to give to the reader an initial framework on how it works and how to, eventually, modify and upgrade it.

### A.1 User Interface

The Graphical User Interface (GUI) of the program is divided in two parts by a vertical separator, the right side containing buttons and controls, the left one displaying the instruments' readings.

When first executed, an initialisation step is needed since the Bentham M300EB had no GPIB query options: only write operations were possible. The user is prompted for the actual settings of the monochromator, i.e. its output wavelength and filter number (Fig.A.1 and Fig.A.2). As explained later, the data will be stored in a global variable file to be used by all the other *LabVIEW Virtual Instruments* (VIs) while maintaining code readability.

#### A.1.1 Main Menus

The user will then find himself on the main menu, displaying navigation buttons on the left and, still unused, calibration and alignment readings from the Lock-In and Multimeter on the right (Fig.A.3). It is possible to choose from here to either stop the execution or move to *Calibration* or *EAB* sections. Furthermore, an e-mail section is present, where address can be set to receive a bulletin message as soon as a measurement finishes executing.

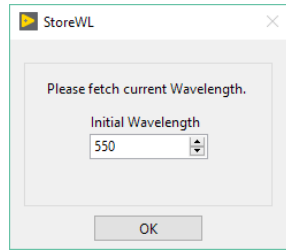


Figure A.1: *Fetch Wavelength* prompt.

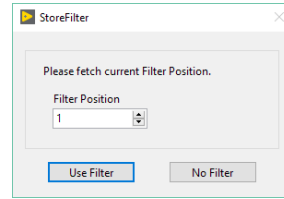


Figure A.2: *Fetch Filter* prompt.

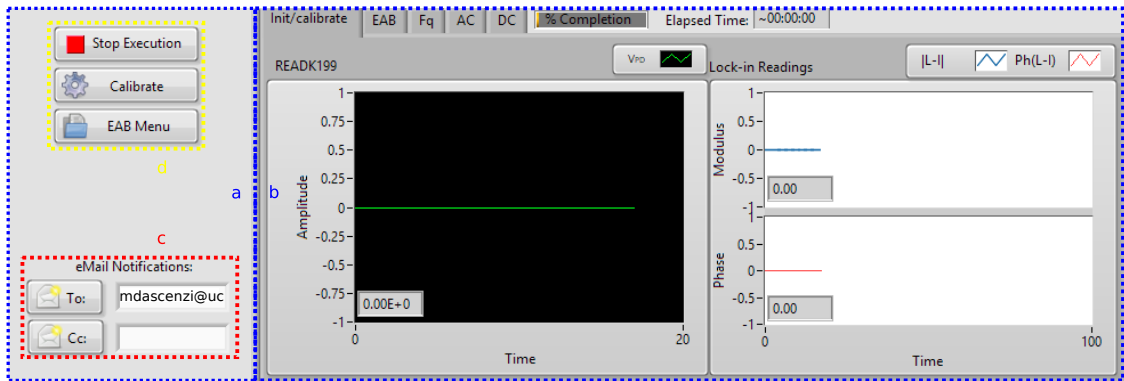


Figure A.3: *Main Menu*. (a), (b): Interface separation (menu buttons, indicators). (c): email menu. (d): navigation buttons.

Pressing the *EAB Menu* button will open the section containing all the EAB-related *Virtual Instruments* that have been created (Fig.A.4). The whole interface was developed in this way so that it could fit other similar programs just by adding new directories.

### A.1.2 Calibration/Alignment Menu

The *Calibration* button will instead allow the user to get a quick idea of the condition of the alignment. This debug menu contains all the controls and indicators needed to check if the instruments are able to discern any decent signal (Fig.A.5).

The controls allow to set, namely:

- the output wavelength of the Monochromator (in  $nm$ );
- the Monochromator's filter slot;
- the Lock-In oscillator's frequency (in  $Hz$ );
- the Lock-In oscillator's AC voltage (in  $V$ );
- the Lock-In oscillator's bias voltage (in  $V$ );

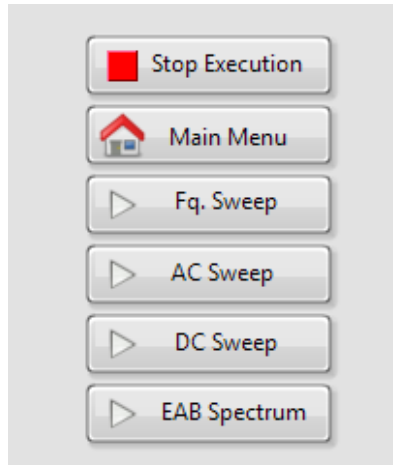


Figure A.4: *EAB Menu* directory, containing all our Virtual Instruments.

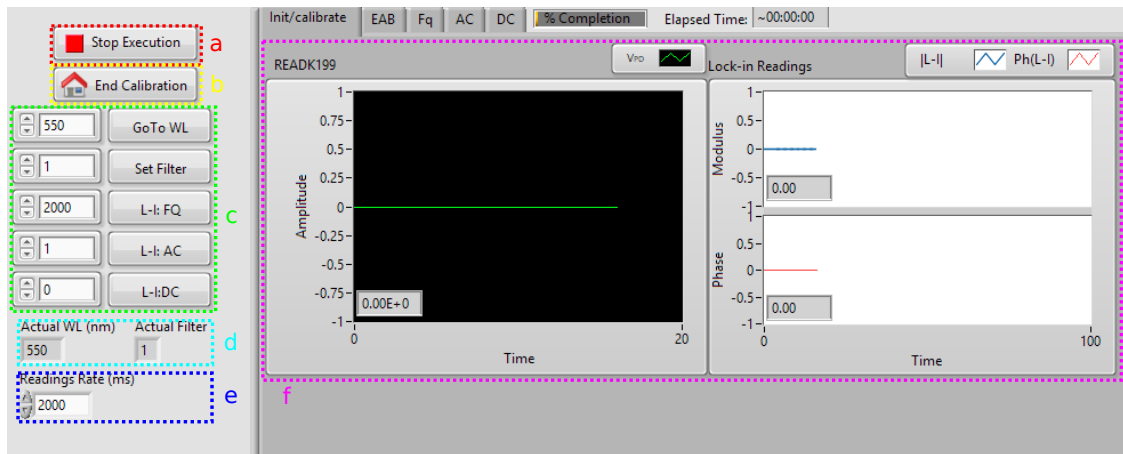


Figure A.5: *Calibration Menu*. (a): Stop button. (b): Home directory button. (c): Lock-In and Monochromator's controls. (d): Monochromator's indicators (WL and filter). (e): *ms* time between readings. (f): Multimeter and Lock-In readings.

- the time-out between each measurement (in *ms*).

The indicators show the Monochromator's settings and the readings from the Multimeter and the Lock-In. These two measurements can be used to determine if anything on the lab table has been put the wrong way or if, with a slight movement of the lenses, of the sample-holder or of the photodetector, the signal magnitude can be improved. This step is crucial for the sake of having reliable results, and doing this every time the sample is changed or the sample older is removed, even if not mandatory, is strongly suggested.

### A.1.3 EAB Spectrum Menu

From this menu it is possible to launch the VI that takes an Electro-Absorption spectra (first and second harmonic) from the sample (Fig.A.6).

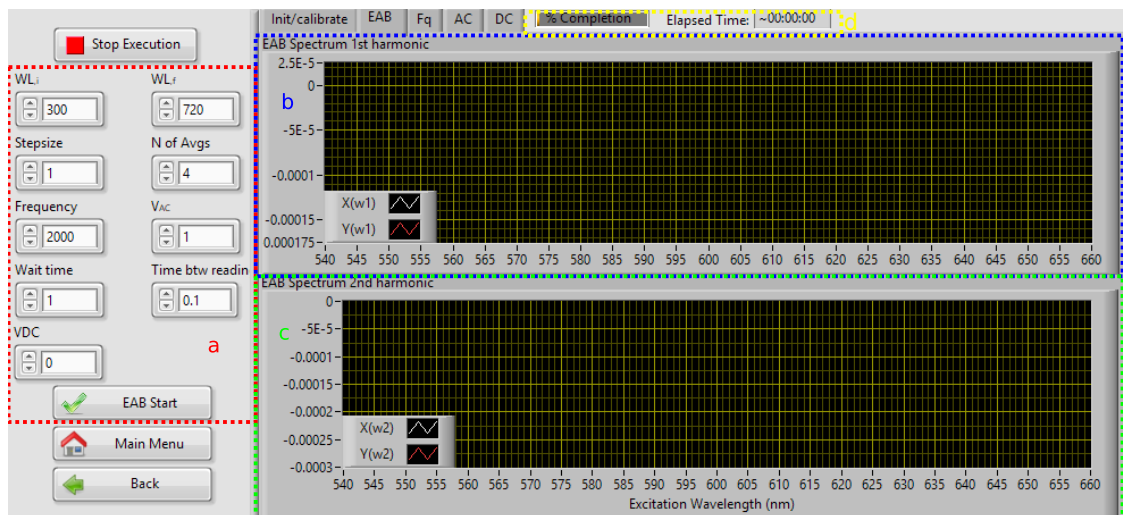


Figure A.6: *EAB spectrum measurement menu*. (a): EAB spectrum control variables. (b): first harmonic electro-absorption output. (c): second harmonic electro-absorption output. (d): Execution status bar and elapsed time.

Displayed on the right are the In-phase and Quadrature Electro-Absorption components. The controls on the left allow to choose as parameters:

- **Initial wavelength, final wavelength and step-size** in  $nm$  of the excitation light beam (an equispaced vector will be generated). As a rule of thumb, since the Monochromator is not completely reliable for frequencies really far from the visible, it is preferable not to cross over the interval between  $300\text{ nm}$  and  $900\text{ nm}$ .
- **Number of measurements** taken for the average. It can cover up for some noise errors, but exceeding 4 repetitions fruitlessly slows down the execution.
- **Lock-In oscillator's Frequency**. The value is usually set to  $2\text{ kHz}$  or kept under  $51\text{ kHz}$  since the second harmonic cannot exceed the  $102\text{ kHz}$  limit of the Lock-In. Even if in principle one could trespass over  $51\text{ kHz}$  for the first harmonic, the results would still be subject to the photodetector frequency dependence, that starts to influence our measurements after around  $45\text{ kHz}$ .
- **Lock-In oscillator's DC bias**. It cannot exceed values over  $\pm 10.5\text{ V}$ , since it is generated by the AUXV2 output of the Lock-In. It is suggested anyway not to stress the devices with a too high voltage for a long period.

- **Lock-In oscillator’s AC component.**  $1 V_{AC}$  is usually enough to achieve a decent SNR for the first harmonic signal.
- **Wait times** between measurements. An amount of time between measurements is already embedded in the program, but the two parameters can be set in case a sample needs a longer settling time (the first one is just considered after a change in the Monochromator, the other one in between each measurement).

When ready, just press *EAB Start*. The bars on top of the instruments readings show the completion percentage and the elapsed time since the start of the measurement and the text file is generated with an automatic name and updated at every step.

### A.1.4 Frequency Sweep Menu

This is a variation of the EAB measurement (Fig.A.7). This time, the frequency is spanned over a logarithmically generated vector and the Wavelength is fixed at every scan.

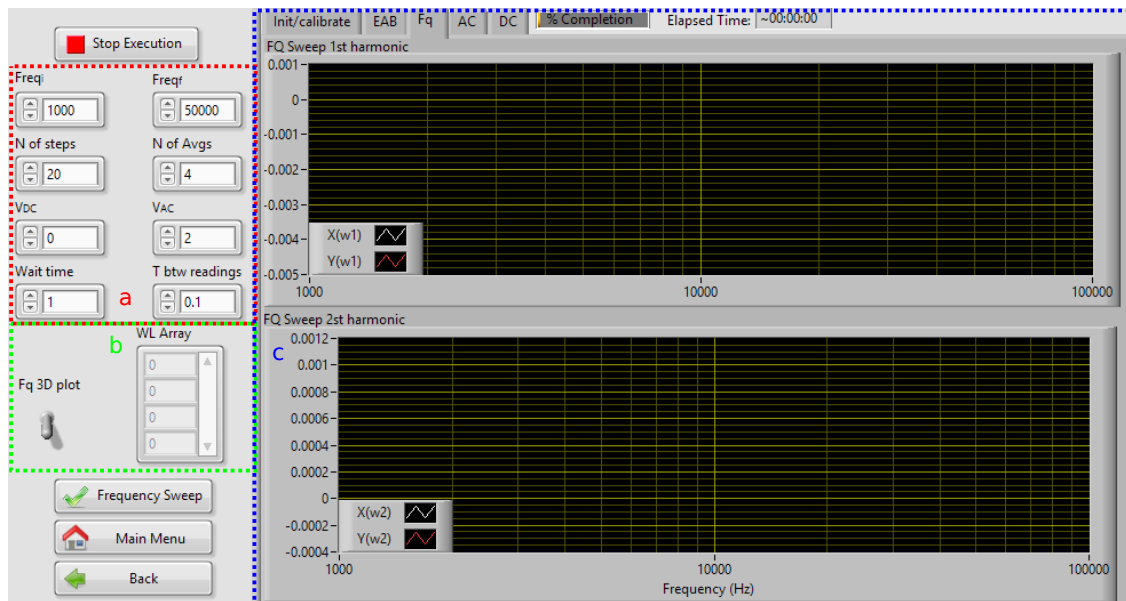


Figure A.7: *Frequency Sweep* measurement menu. (a): Frequency Sweep control variables. (b): Wavelength generator and selector. (c): electro-absorption output (the abscissa scale is logarithmic).

The controls and suggestions are similar to all the other sweeps with few exceptions. The parameter’s (now a Frequency) vector is logarithmically spaced, and usually set to have 15 or 20 steps between  $1 kHz$  and  $50 kHz$ . The settle

times along this vector are usually faster with respect to the other programs. The Wavelengths are chosen from an arbitrary look-up-table of which its first element is automatically set to the magnitude peak of the EAB spectra, if previously executed. There is anyway another way to define this list. By default, the table where to insert the desired Wavelengths is displayed; otherwise, by activating the *3D Plot* switch, one can also choose to generate a linear space for the Wavelength vector (Fig.A.8). As shown in 3.2.1, this tool can give us a good insight on the structure’s frequency response at different photon energies.

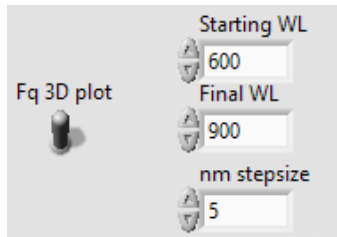


Figure A.8: *3D Plot control* (activated switch) and linear vector generation.

This time the graph will only display a single Wavelength at a time, but the text file will contain all the scans’ results.

### A.1.5 AC Sweep Menu

The options of this program are analogous to the previous one’s (Fig.A.9). The sine amplitude lower bound is  $4\text{ mV}_{RMS}$  ( $6\text{ mV}$ , circa) for the Lock-In and will be clipped if trying to set it to a lower value. It can go up to  $5\text{ V}_{RMS}$ , if needed and if the device is healthy enough (low input impedance  $R_{in}$  and high  $V$  values can trigger the Mixer’s output protection). Please note that the inserted number has to be the value of the *peak voltage*, not the *RMS*.

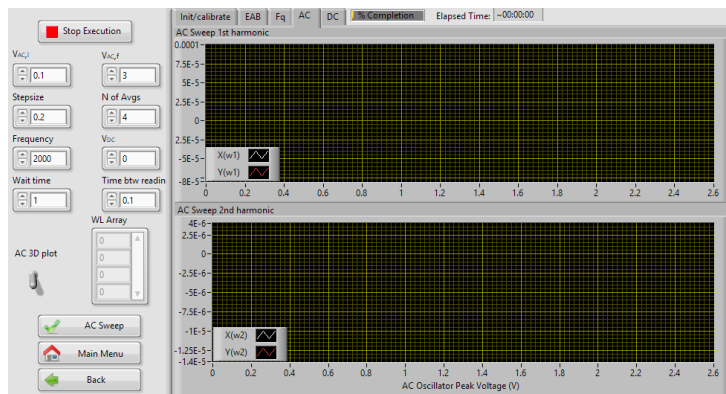


Figure A.9: *AC Sweep* measurement menu.

### A.1.6 DC Sweep Menu

As already stated, DC bias values can reach  $\pm 10.5$  V. The usual procedure is to set the Wavelength near to the excitonic peak and look at the behaviour of the Electro-Absorption signal by letting the DC Voltage approach zero, starting from a negative bias. By fitting this to a line, one can find its zero-crossing value, that is a good approximation of the Built-In Voltage of the structure, as shown in section 2.3.

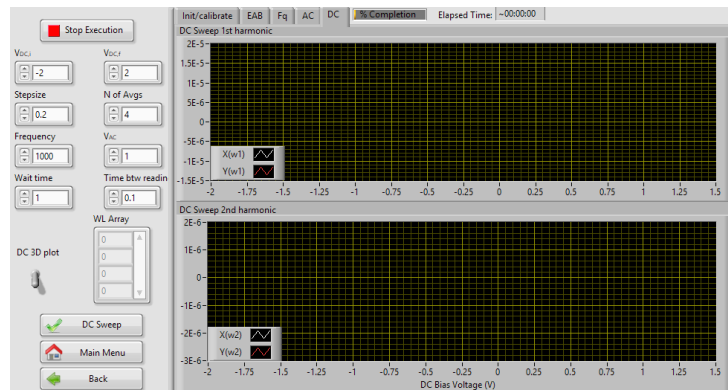


Figure A.10: *DC Sweep* measurement menu.

## A.2 LabVIEW Scripts: EAB Measurements

### A.2.1 Front Panel

In order to embed different measurement routines in a single VI with a directory structure, a State Machine [40] controlled by Event Structures [41] was employed in LabVIEW. An elementary example of this kind of structure can be seen in Fig. A.11, where all the necessary blocks have been used. The appearance of the menus has already been shown in section A.1, whilst in Fig. A.12 the complete flow chart of the state machine is displayed. At almost every moment except during measurements, in brief, our program is just idle and expecting an interrupt request through an event structure in order to move to a different state.

When the program starts, the first state to be executed is *initialise* (Fig. A.13), where the current Wavelength and Filter values of the Monochromator are fetched by the user, then the Multimeter and Lock-In are initialised to the right settings (every subVI's content will be described in section A.3). The next state (*idle*, i.e. the main menu) goes then inside a shift register that will feed it back to the new iteration of the loop.

As in every state transition, all the controls are hidden prior to toggling the visibility of the needed ones only (Fig. A.13). This is done by grouping the buttons'

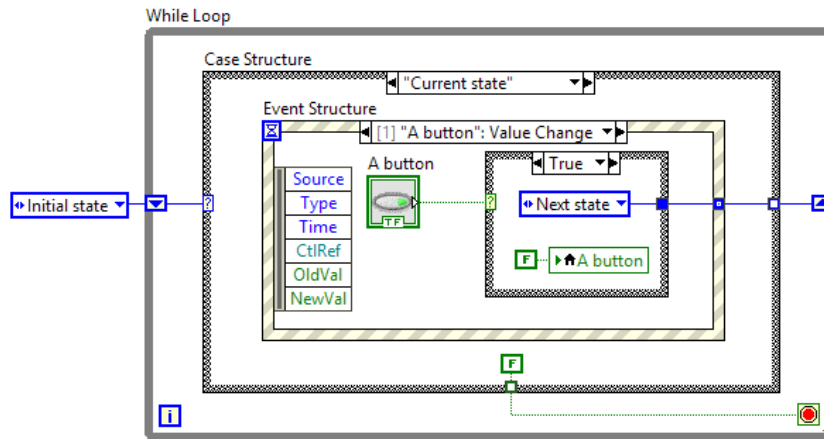


Figure A.11: Simple SM example. The *while loop* executes until the *stop* is triggered. The *case structure* determines the instructions based on **Current state** (set to **Initial state** on the first run) and then (optionally, with the aid of an *event structure*) the outputs and **Next state** are selected. An *event* can be triggered in this case by the toggling of a button.

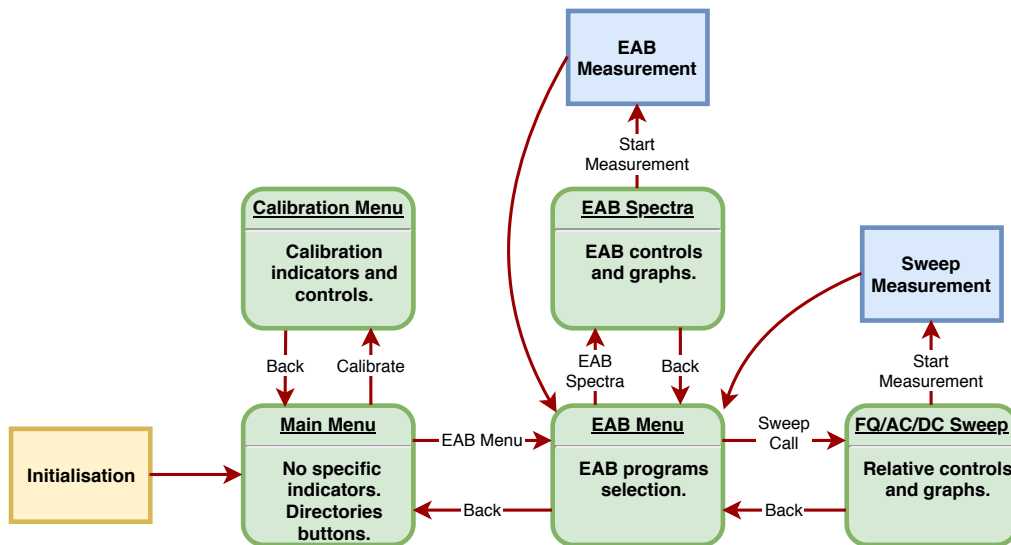


Figure A.12: Menus state machine flow chart.

references in an array (Fig.A.14) and using them to change their *visible* property bit one by one (Fig.A.13(e), Fig.A.15). The error connection in Fig.A.13(e) is used to force the order of execution.

Both in *idle* (main menu) and in *EAB Menu*, the program just keeps waiting for a button to toggle and, depending on which one, an event to be triggered. Once the event is selected some code, if needed, will be executed and a precise state will

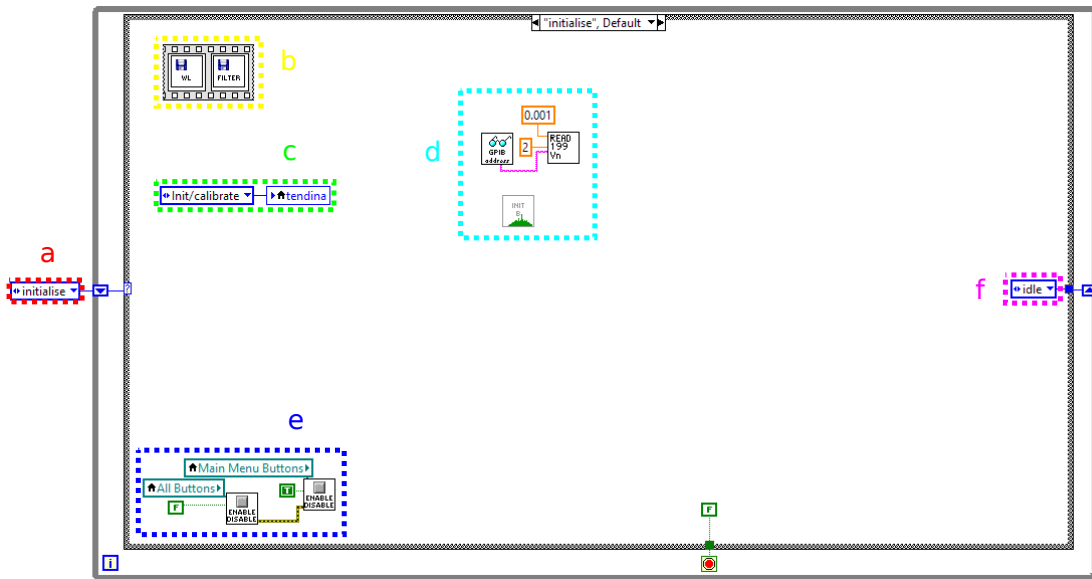


Figure A.13: *Initialise* state. (a): First state entering the loop. (b): Wavelength and Filter Number prompts. (c): Drop down menu (indicators-side) control. (d): Instruments' initialisation. (e): Buttons visibility handling. (f): Next state being fed back.

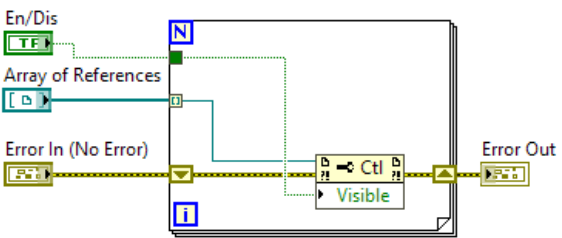
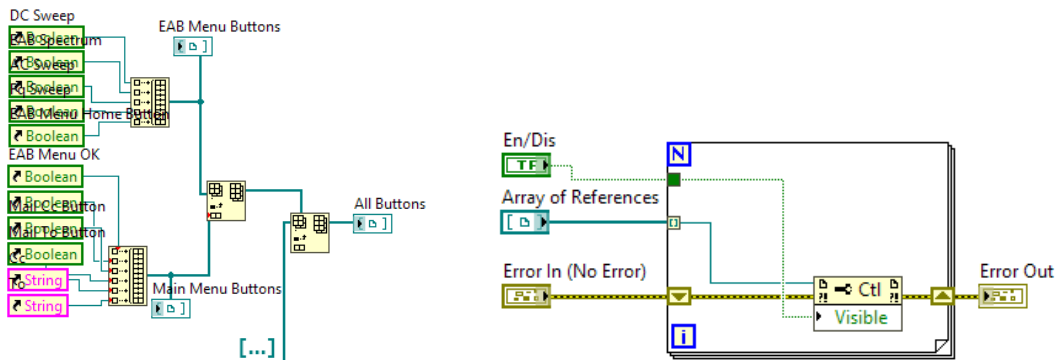


Figure A.14: References' array creation. Figure A.15: *Enable/Disable* snippet.

be looped back. In Fig.A.16, for example, the *Calibrate* button has been pushed, so the program will move to its namesake state.

There are few exceptions to this behaviour on the main menu. One of those concerns the e-mail feature of the program. When the *To:* (or *Cc:*) button is pressed, the mail's recipient (or *Cc*) is updated with the one that is written on the control and will be used later, when a measurement finishes executing, to send a bulletin message (Fig.A.3(c), Fig.A.17, Fig.A.20(e)).

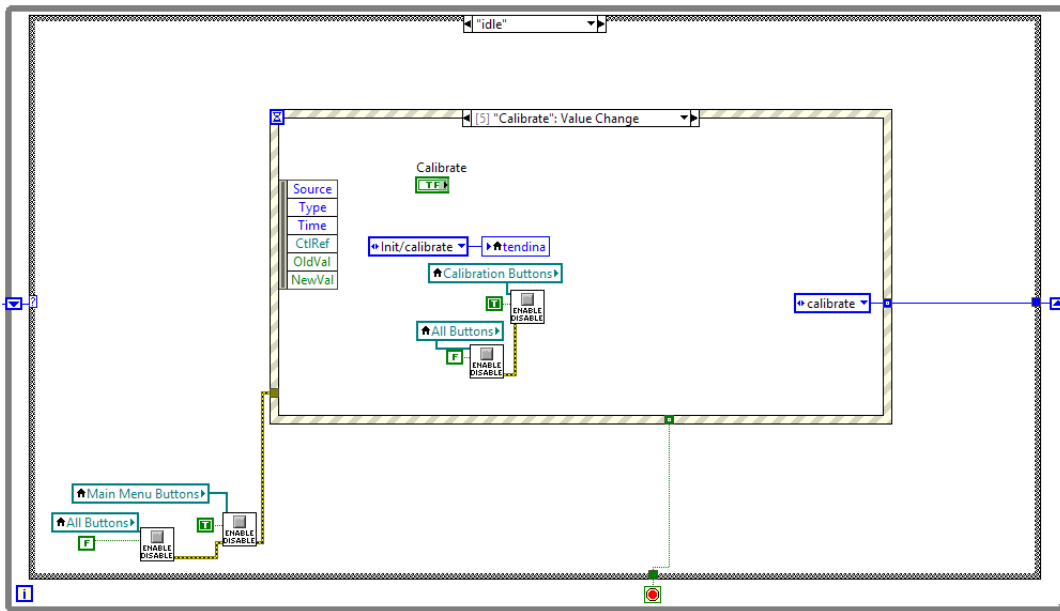


Figure A.16: When *Calibrate* is pushed, the program moves in the calibration menu.

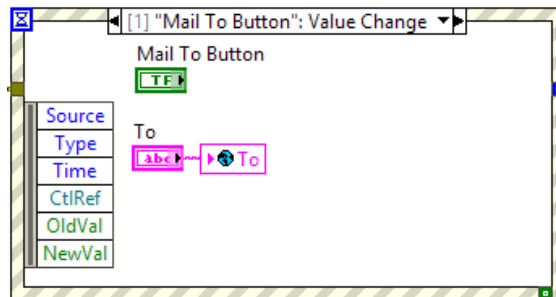


Figure A.17: Update of global variable containing the e-mail's recipient.

## A.2.2 Calibration

The calibration menu has no longer a directory function, but allows to drive and read the instruments with specific GPIB calls. Firstly, the controls (Fig.A.5(c)) can be used to set the Monochromator or the oscillator parameters, *i.e.* all the inputs of our sample (Fig.A.18). The readings from the instruments will then be displayed (Fig.A.5(f)), with a cadence that is dictated by the event timeout control (Fig.A.5(e), Fig.A.19). This time, no button controls can be put in this section of the SM, since the timeout's presence would cause them to flicker continuously.

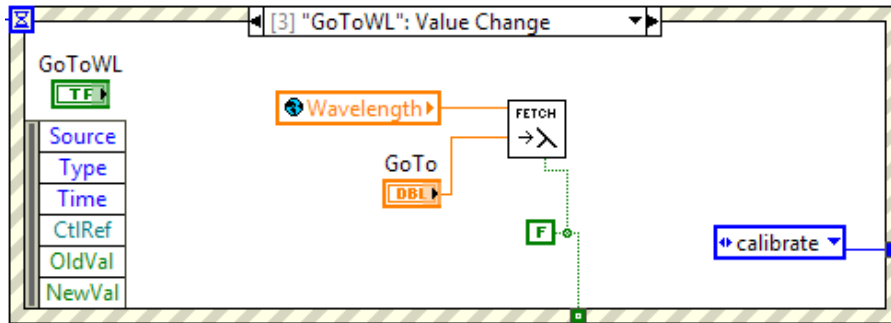


Figure A.18: Monochromator's Wavelength change.

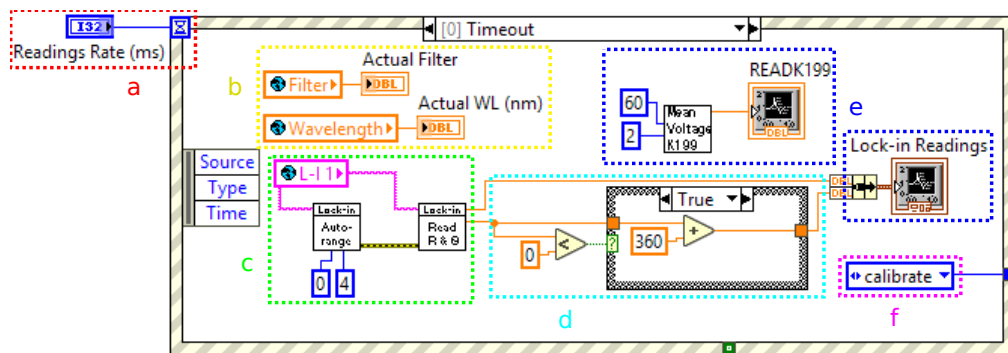


Figure A.19: Calibrate timeout event. (a): Instruments scan interval, if no button has been pressed at that *ms* timer expiry, a measurement is triggered. (b): Monochromator's indicators update. (c): Lock-In Auto-range and modulus and phase measurement. (d): Phase wrap. (e): Graphs update. (f): Next state is still *Calibrate*.

### A.2.3 EAB Spectrum

The EAB spectrum measurement can be launched from its menu (Fig.A.6). All the controls and graph's references will become the EAB subVI's inputs (the Wavelengths vector is generated directly inside the program). After its execution, in addition to the writing of the dump file, the Wavelength that is associated to the magnitude peak is automatically saved for the other measurements and an e-mail can be sent, if configured (Fig.A.20).

The subVI (Fig.A.21) starts with the inputs reading (and the generation of an equispaced vector). These will be used to generate the instruments' controls and the file's name and header. Then, the file is automatically created, the elapsed time counter is reset and all the instruments are initialised and set to the desired outputs.

At every iteration of the loop, the Wavelength of the Monochromator is changed and the status bars on the front panel are updated. Then, the measurements are

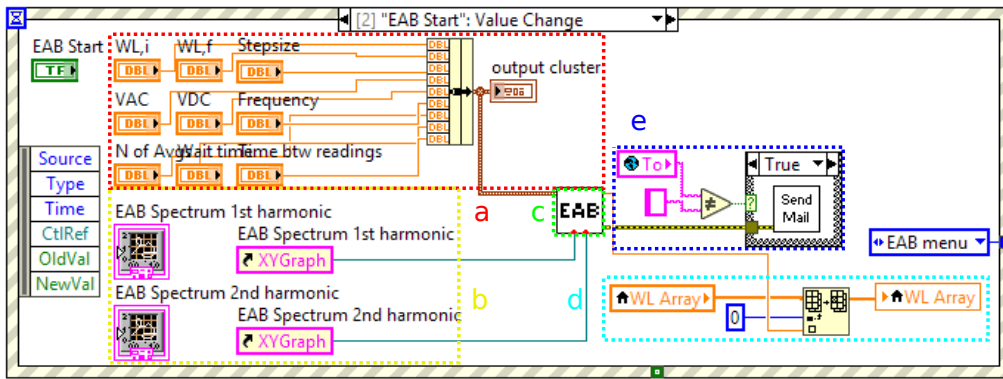


Figure A.20: EAB Start event. (a): Measurements controls are grouped into a cluster. (b): Graphs are passed by reference to the subVI. (c): The EAB subVI is executed. (d): The peak’s wavelength is appended to the wavelength vector used by the sweep measurements. (e): An e-mail is sent, if configured.

taken (after an auto-range round for both the Lock-Ins) and the file and the graphs are updated.

After the loop is completed, the oscillator and its DC bias are set to zero in order not to stress the device and the peak wavelength is evaluated from the measured data.

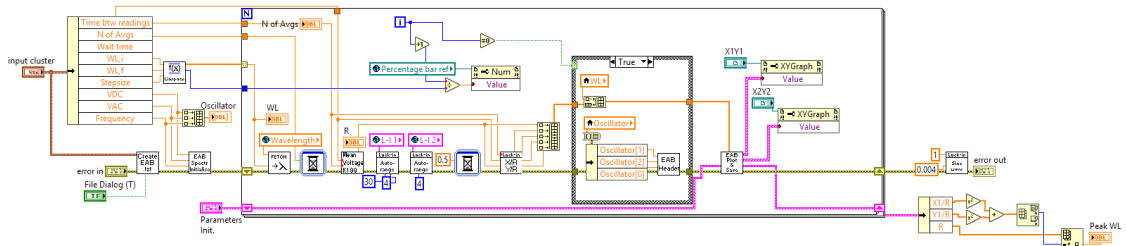


Figure A.21: EAB Spectrum measurement subVI.

### A.2.4 Fq/AC/DC Sweeps

As already explained in Section A.1.4, there are not many differences between Spectrum and Sweep routines, one of them being the fact that the latter can take measurement over two parameters, thus generating a 3D plot. As shown in Fig.A.22(a), Fig.A.8 and Fig.A.7, the 3D button can toggle between an auto-generated or a user-produced Wavelength array, that will sum up with the one related to the sweep parameter (in the figures, the frequency).

The buttons’ handling is now slightly different. Another subVI has been added in order to take into account the different type of the addresses in the array (it



and file handling are almost identical, but this time two loops have to be present instead of one. In order to optimise the speed of the process, the inner loop is the one with the Frequency parameter spanning, so that the program will not waste time waiting for the bulky Monochromator to change its wavelength.

## A.3 LabVIEW Scripts: GPIB Libraries

All the communications between instruments were handled by an IEEE-488 interface (GPIB), connected to the computer with a National Instruments GPIB-USB-HS adapter. All the scripts are referencing low-level GPIB functions in their subVIs, since all the instruments were old enough not to have LabVIEW drivers provided by NI.

All the instrument calls are quite similar amongst all the VIs, thus it is better to just show the more complex ones, while describing the others in terms of GPIB commands.

### A.3.1 Monochromator

The Bentham TMc300 Monochromator [42] has only few options in its command list, since the only job it has is to change its output wavelength and filter. All the VIs are inside a library, *Bentham M300EB (PMC38).llb*

The wavelength is set by sending an increment or decrement interval via the GPIB, thus its initial position is needed. The filter follows the same approach, but it only has 6 positions, each one corresponding to some physical filter glass and a shutter.

**User Prompts** *Save Wavelength.vi* and *Save Filter.vi* prompt the user for a numerical value, then save it in two global variables. Regarding the filter, it is possible not to use it: in that case, it will be automatically moved to the 1<sup>st</sup> position. The two global variables will be called, then overwritten, while modifying the monochromator's status.

**GoToWavelength/Filter** *GoToWavelength.vi* and *GoToFilter.vi* evaluate the step size to reach the selected value and use the GPIB to set it. The commands are structured in this way: 1 Byte for the increasing or decreasing direction (I/D), 4 Bytes indicating the interval magnitude in  $\frac{1}{20} nm$  or number of filter steps, 1 Byte specifying if wavelength (W) or filter (T) has to be changed.

**Wavelength to Filter** In *Wavelength-Filter.vi*, a filter able to cut values of wavelengths shorter than the selected one is chosen from a look-up table. This will

drastically reduce the harmonic content of our light, since the  $\lambda/2$  value is likely to come out less attenuated from the monochromator.

### A.3.2 Lock-In

The MODEL SR830 DSP Lock-In Amplifier [43], amongst the others, has a slightly more complex role and it needs extra care. Starting from the oscillator commands, it also needs different types of readings and an articulated full-scale range calibration.

**Buffer Flush** *Lock-in Buffer Flush.vi* is the first one to be executed, during initialisation. an `*IDN?` command is queried, then the output is read in a for loop until we receive back the instrument's name. This was the only way to safely flush the instrument's buffer without having to wait for a GPIB timeout.

**Oscillator Instructions** *Lock-in FMOD & HARM auto.vi* sets L-I1 to FMOD1 (internal oscillator as reference signal) and HARM1 (lock to first harmonic). L-I2 receives instead FMOD0 (external reference) and HARM2. It is also executed during an initialisation. After that we can use *Lock-in Oscillator Control.vi*, *Lock-in Oscillator Fq.vi*, *Lock-in Oscillator DC.vi* or *Lock-in Oscillator AC.vi* to set the values of every (with the former) or only one parameter. FREQX sets the sine frequency to X Hertz, SLVLX sets the AC voltage to X  $V_{RMS}$ , converted from Volt beforehand. AUXV2, X sets the auxiliary output to X Volt (since the mixer will invert the signal, the requested value is multiplied by  $-1$  inside the VI).

**Reading the Instrument** The Lock-In reading can be interpreted in terms of Modulus and Phase ( $R$  and  $\phi$ ) or In-Phase and Phase-Quadrature ( $X$  and  $Y$ ) components. The  $X$  and  $Y$  measurements are obtained by mixing the photodiode output with the oscillator and its  $90^\circ$  shifted signal, then they can be converted by their relation:

$$R = \sqrt{X^2 + Y^2} \quad \phi = \text{atan2}(X, Y), \quad (\text{A.1})$$

where  $\text{atan2}(X, Y)$  is the 2-argument arctangent of  $X$  and  $Y$ . *Lock-in Read x&y.vi* and *Lock-in Read R&Theta.vi* all use the command `OUTP?X`, where X is the channel number (1:  $X$ , 2:  $Y$ , 3:  $R$ , 4:  $\phi$ ). Another version is used in the program (*Lock-in X/T Y/T.vi*) that reads the  $X$  and  $Y$  signals from both the Lock-Ins and divides them by  $T$ , as in section 2.1.

### A.3.3 Multimeter

The Keithley Model 199 GPIB drivers are a slightly modified version of the available ones [44, 45]. *K199 Complete.vi* is first used to initialise the instrument's input mode and channels, then *K199 Read Mean.vi* takes an averaged measurement of

the chosen channel. The number of averages can be chosen, but has been set to only three since the instrument already has a solid resolution.

### A.3.4 Global Variables

When a variable has to be shared between more functions in the same VI, LabVIEW provides the *local variable* structure to easily provide that value where it is needed. But as the program’s structure gets increasingly elaborate and the hierarchy levels increase, *global variables* could be necessary to efficiently handle the common parameters, such as GPIB addresses.

Since every GPIB subVI needs an instrument address, and most of them are tailored for specific instruments, it is easier to have all of them grouped in the same section of the code, and let a memory call read for that value, instead of having the same number repeated in every VI.

Global variables are a more basic kind of VI that can only act as a pointer for memory locations. By using this pointer, we can access and read/write that parameter even if the call comes from a different VI from the one that previously wrote/read it.

*GPIB\_Addresses\_Global.vi* is used to collect all the pointers to GPIB addresses, that also have to be written at execution time by *GPIB\_Addresses.vi*. In this way, just by modifying the latter we can correct for a change in an instrument address.

*Globals\_Instruments.vi* contains instead all the instruments of the parameters, such as the monochromator and the lock-in set parameters.

Another VI, *Globals\_Files.vi*, takes care of the saving of the files, and their folders.

## A.4 Post-Processing and Plotting Scripts

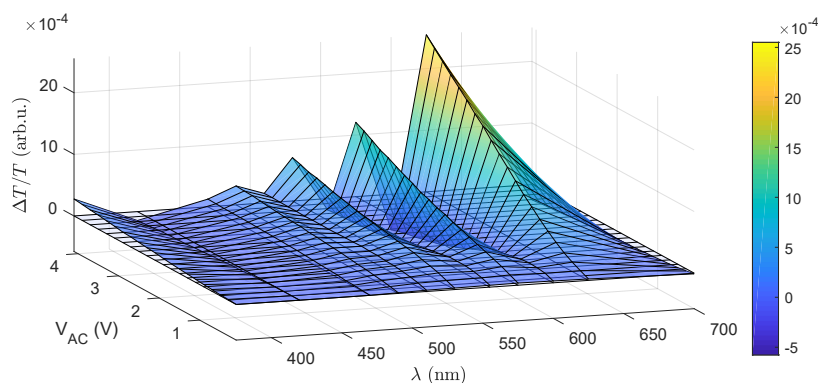


Figure A.24: An AC Sweep of P3HT:PCBM with annealed PEDOT:PSS plotted with MATLAB script.

Most of the figures in this thesis have been made by using OriginPro plotting tools. Anyway, also a MATLAB script for plotting has been written, in order to automate the process. In this way, we just need to open a file with the script and MATLAB will produce some scatter plots and a 3D plot (Fig.A.24). When started, it also give the option to select some wavelengths to be individually plotted.

It has been tested with all the sweep *.txt* dumps, but it is not suited for EA spectrum files. Here is the code, converting the files in a tabular and plotting them:

```
1 close all
2 clear all
3
4 [filename, folder] = uigetfile('.txt');
5 if filename == 0
6     disp('canceled operation')
7     return
8 end
9 dat = datastore(strcat(folder, filename));
10 T = read(dat); %stores filename in a tabular
11 T = sortrows(T, [1,3]); %sorts by wavelength, then by sweep
    param.
12
13 [gNum, wl, fq] = findgroups(T.Wavelength_nm_, T.(3));
14 [gNum1, wl1] = findgroups(T.Wavelength_nm_);
15 [gNum2, fq2] = findgroups(T.(3)); %T.(3) is the sweep
    parameter
16 T.abs1 = sqrt(T.X1_R.^2+T.Y1_R.^2); %evaluate modulus
17
18 %% Scatter Plots
19 figure
20 hold on
21 if(strcmp(T.Properties.VariableNames{3}, 'Freq_Hz_'))
22     set(gca, 'XScale', 'log')
23 end
24 splitapply(@plot, T.(3), T.X1_R, gNum1)
25 grid on
26 grid minor
27 ylabel('$\Delta T/T$ (arb.u.)', 'interpreter', 'latex')
28 xlabel(T.Properties.VariableNames{3}(1:3))
29
30 figure
31 scatter(T.(3), T.abs1, 10, T.Wavelength_nm_)
32 %contour3(T.Wavelength_nm_, T.Freq_Hz_, T.X1_R)
```

```

33 if(strcmp(T.Properties.VariableNames{3}, 'Freq_Hz_'))
34     set(gca, 'XScale', 'log')
35 end
36 grid minor
37 grid on
38 ylabel('$\Delta T/T$ (arb.u.)', 'interpreter', 'latex')
39 xlabel(T.Properties.VariableNames{3}(1:3))
40
41 %% 3D Plot
42 jj = histcounts(gNum1); %number of discrete frequencies
43 k = 1;
44 Z = zeros(length(wl1), jj(1)); %initialise space matrix
45 for i=1:length(wl1)
46     for j=1:jj(1)
47         Z(i, j) = T.X1_R(k);
48         k = k+1;
49     end
50 end
51
52 figure
53 s = surf(wl1, fq2, Z, 'FaceAlpha', 0.6, 'FaceColor', 'Interp');
54 hold on
55 p = surf(wl1, fq2, zeros(length(fq2), length(wl1)), 'FaceAlpha',
56     , 0.1);
57 if(strcmp(T.Properties.VariableNames{3}, 'Freq_Hz_'))
58     set(gca, 'YScale', 'log')
59 end
60 colorbar
61 axis tight
62 zlabel('$\Delta T/T$ (arb.u.)', 'interpreter', 'latex')
63 ylabel(T.Properties.VariableNames{3}(1:3))
64 xlabel('$\lambda$ (mm)', 'interpreter', 'latex')
65 WLplot = input(strcat('Which Wavelengths do you want to plot
66     separately?\n' ...
67     , '(use square parentheses and comma if more than one):\n'
68     , 'n'));
69 if(not(isempty(WLplot)))
70     figure
71     scatter(T.(3)(any((T.Wavelength_nm==WLplot), 2)), ...
72         T.X1_R(any((T.Wavelength_nm==WLplot), 2)), 10, ...

```

```
71         T.Wavelength_nm_(any((T.Wavelength_nm_==WLplot),2))
72         )
73     if(strcmp(T.Properties.VariableNames{3}, 'Freq_Hz_'))
74         set(gca, 'XScale', 'log')
75     end
76     grid minor
77     grid on
78     legend(num2cell(wl1(any((wl1==WLplot),2))'))
79 end
```



# Bibliography

- [1] A. G. MacDiarmid, “Synthetic metals: A novel role for organic polymers (Nobel lecture),” *Angewandte Chemie International Edition*, vol. 40, no. 14, pp. 2581–2590. [Online]. Available: <https://onlinelibrary.wiley.com/doi/abs/10.1002/1521-3773%2820010716%2940%3A14%3C2581%3A%3AAID-ANIE2581%3E3.0.CO%3B2-2>
- [2] T. A. Skotheim, *Handbook of conducting polymers*. CRC press, 1997.
- [3] A. Dodabalapur, “Organic light emitting diodes,” *Solid State Communications*, vol. 102, no. 2, pp. 259 – 267, 1997, highlights in Condensed Matter Physics and Materials Science. [Online]. Available: <http://www.sciencedirect.com/science/article/pii/S0038109896007144>
- [4] C.-M. Lai, Y.-H. Yeh, and Y.-H. Huang, “Pixel structure of active matrix organic light-emitting diode and method for fabricating the same,” Jul. 5 2007, uS Patent App. 11/308,015.
- [5] OLED-Info. Organic electronics growth chart. [Online]. Available: <https://www.oled-info.com/organic-electronics-growth-chart-nanomarkets-2009>
- [6] V. Bodrozic, M. Roberts, N. Phillips, J. Burroughes, S. Mian, and F. Cacialli, “The influence of subgap features in the electromodulation and built-in voltage measurements of polyfluorene blue light-emitting diodes with anodic charge injection layers,” *Journal of Applied Physics*, vol. 101, pp. 084 507 – 084 507, 05 2007.
- [7] T. M. Brown, R. H. Friend, I. S. Millard, D. J. Lacey, T. Butler, J. H. Burroughes, and F. Cacialli, “Electronic line-up in light-emitting diodes with alkali-halide/metal cathodes,” *Journal of Applied Physics*, vol. 93, no. 10, pp. 6159–6172, 2003. [Online]. Available: <https://doi.org/10.1063/1.1562739>
- [8] V. Bodrozic, M. Roberts, N. Phillips, J. Burroughes, S. Mian, and F. Cacialli, “The influence of subgap features in the electromodulation and built-in voltage measurements of polyfluorene blue light-emitting diodes with anodic charge injection layers,” *Journal of Applied Physics*, vol. 101, pp. 084 507 – 084 507, 05 2007.
- [9] M. E. Ziffer, J. C. Mohammed, and D. S. Ginger, “Electroabsorption spectroscopy measurements of the exciton binding energy, electron-hole reduced effective mass, and band gap in the perovskite  $\text{CH}_3\text{NH}_3\text{PbI}_3$ ,”

- ACS Photonics*, vol. 3, no. 6, pp. 1060–1068, 2016. [Online]. Available: <https://doi.org/10.1021/acsphotonics.6b00139>
- [10] T. M. Brown, “Electroabsorption investigations of polymer light-emitting diodes with efficient electrodes,” Ph.D. dissertation, St. John College, Cambridge, 2001.
- [11] O. Abdulrazzaq, V. Saini, S. Bourdo, E. Dervishi, and A. S. Biris, “Organic solar cells: A review of materials, limitations, and possibilities for improvement,” *Particulate Science and Technology*, vol. 31, 09 2013.
- [12] J. D. Myers and J. Xue, “Organic semiconductors and their applications in photovoltaic devices,” *Polymer Reviews*, vol. 52, no. 1, pp. 1–37, 2012. [Online]. Available: <https://doi.org/10.1080/15583724.2011.644368>
- [13] Z. Guan, H.-W. Li, J. Zhang, Y. Cheng, Q. Yang, M.-F. Lo, T.-W. Ng, S.-W. Tsang, and C.-S. Lee, “Evidence of delocalization in charge-transfer state manifold for donor:acceptor organic photovoltaics,” *ACS Applied Materials & Interfaces*, vol. 8, no. 33, pp. 21 798–21 805, 2016, pMID: 27482867. [Online]. Available: <https://doi.org/10.1021/acsami.6b06010>
- [14] S.-W. Tsang, S. Chen, and F. So, “Energy level alignment and sub-bandgap charge generation in polymer:fullerene bulk heterojunction solar cells (adv. mater. 17/2013),” *Advanced Materials*, vol. 25, no. 17, pp. 2433–2433. [Online]. Available: <https://onlinelibrary.wiley.com/doi/abs/10.1002/adma.201370113>
- [15] A. Zampetti, “Heterostructure and interface layers in bulk heterojunction polymer solar cells,” Ph.D. dissertation, University of Rome "Tor Vergata", 2011.
- [16] Wikimedia contributors. (2009) Pi-Bond — Wikipedia, the free encyclopedia. [Online]. Available: <https://en.wikipedia.org/wiki/File:Pi-Bond.svg>
- [17] PhotonicsWiki. (2010) Synthesis of organic semiconductors. [Online]. Available: [http://photonicswiki.org/index.php?title=Synthesis\\_of\\_Organic\\_Semiconductors](http://photonicswiki.org/index.php?title=Synthesis_of_Organic_Semiconductors)
- [18] C. Cobet, J. Gasiorowski, D. Farka, and P. Stadler, *Polarons in Conjugated Polymers*. Cham: Springer International Publishing, 2018, pp. 355–387. [Online]. Available: [https://doi.org/10.1007/978-3-319-75895-4\\_16](https://doi.org/10.1007/978-3-319-75895-4_16)
- [19] David Harvey. Singlet and triplet states. [Online]. Available: <https://community.asdlib.org/imageandvideoexchangeforum/2013/07/30/singlet-and-triplet-states/>
- [20] I. D. Johnson and M. W. Davidson. Jablonski energy diagram - java tutorial. [Online]. Available: <https://www.olympus-lifescience.com/en/microscope-resource/primer/java/jablonski/jabintro/>
- [21] Tokio Chemical Industry CO. Organic solar cell (opv) materials. [Online]. Available: [https://www.tcichemicals.com/eshop/en/be/category\\_index/12802/](https://www.tcichemicals.com/eshop/en/be/category_index/12802/)
- [22] D. S. Ginley and D. Cahen, *Fundamentals of materials for energy and environmental sustainability*. Cambridge university press, 2011.

- 
- [23] Z. He, C. Zhong, S. Su, M. Xu, H. Wu, and Y. Cao, “Enhanced power-conversion efficiency in polymer solar cells using an inverted device structure,” *Nature photonics*, vol. 6, no. 9, p. 591, 2012.
- [24] L. Bernini, “Caratterizzazione di film sottili di pedot:pss,” Ph.D. dissertation, Università di Bologna, 2014.
- [25] A. Chen, K. Zhu, Q. Shao, and Z. Ji, “Understanding the effects of tco work function on the performance of organic solar cells by numerical simulation,” *Semiconductor Science and Technology*, vol. 31, no. 6, p. 065025, 2016.
- [26] S. Viticoli and M. Muccini, “L’opportunità di sviluppare in Italia il fotovoltaico di terza generazione,” *White Paper*, 2010.
- [27] Ossila Ltd. Solar cells: A guide to theory and measurement. [Online]. Available: <https://www.ossila.com/pages/solar-cells-theory>
- [28] S. Kuno, H. Akeno, H. Ohtani, and H. Yuasa, “Visible room-temperature phosphorescence of pure organic crystals via a radical-ion-pair mechanism,” *Phys. Chem. Chem. Phys.*, vol. 17, pp. 15 989–15 995, 2015. [Online]. Available: <http://dx.doi.org/10.1039/C5CP01203A>
- [29] W. Knoll and R. C. Advincula, *Functional Polymer Films, 2 Volume Set*. John Wiley & Sons, 2013.
- [30] S. J. Martin, H. L. Anderson, and D. D. C. Bradley, “Quadratic electro-optic non-linearity of a conjugated porphyrin polymer measured in the q-band one-photon resonance region,” *Advanced Materials for Optics and Electronics*, vol. 4, no. 4, pp. 277–283. [Online]. Available: <https://onlinelibrary.wiley.com/doi/abs/10.1002/amo.860040407>
- [31] R. P. Feynman, R. B. Leighton, and M. Sands, “Lectures on physics, vol. 2,” *Addison-Wesley Publishing Company, ODD*, pp. 32–1 to 32–13, 1965.
- [32] I. Almog, M. Bradley, and V. Bulovic. (2011, Spring) Electromagnetic energy. Massachusetts Institute of Technology: MIT OpenCourseWare. [Online]. Available: <https://ocw.mit.edu>
- [33] P. N. Butcher and D. Cotter, *The elements of nonlinear optics*. Cambridge university press, 1991, vol. 9.
- [34] R. W. Boyd, *Nonlinear Optics, Third Edition*, 3rd ed. Orlando, FL, USA: Academic Press, Inc., 2008.
- [35] Solar Light Company, Inc. SL-03730 300 watt ozone-free short arc xenon lamp. [Online]. Available: <https://solarlight.com/product/sl-03730-300-watt-ozone-free-short-arc-xenon-lamp/>
- [36] K. Beck, M. Beedle, A. van Bennekum, A. Cockburn, W. Cunningham, M. Fowler, J. Grenning, J. Highsmith, A. Hunt, R. Jeffries, J. Kern, B. Marick, R. C. Martin, S. Mellor, K. Schwaber, J. Sutherland, and D. Thomas, “Manifesto for agile software development,” 2001. [Online]. Available: <http://www.agilemanifesto.org/>
- [37] Nicholas Iivanecky. Crash article in agile development. [Online]. Available: <https://medium.com/open-product-management/>

- [crash-article-in-agile-development-da960861259e](#)
- [38] Y. Kim, A. M. Ballantyne, J. Nelson, and D. D. Bradley, “Effects of thickness and thermal annealing of the pedot:pss layer on the performance of polymer solar cells,” *Organic Electronics*, vol. 10, no. 1, pp. 205 – 209, 2009. [Online]. Available: <http://www.sciencedirect.com/science/article/pii/S156611990800178X>
  - [39] L. E. Scriven, “Physics and applications of dip coating and spin coating,” *MRS Proceedings*, vol. 121, p. 717, 1988.
  - [40] (2008) National Instruments White Papers: Using a state machine (event driven) architecture. [Online]. Available: <http://www.ni.com/white-paper/2926/en/>
  - [41] (2008) National Instruments White Papers: Event-driven programming in labview. [Online]. Available: <http://www.ni.com/white-paper/3331/en/>
  - [42] *Single Monochromator*, Bentham, 1993, rev. 2.5.
  - [43] *DSP Lock-In Amplifier*, Stanford Research Systems, 1993, rev. 2.5.
  - [44] (2015) National Instruments White Papers: LabView library example for k199. [Online]. Available: <https://doc.xdevs.com/article/keithley-instruments/>
  - [45] *System DMM Scanner*, Keythley, 1987, rev. D.